Symmetry manipulation of nonlinear optical effect for metallic transition-metal dichalcogenides

Ren Habara [1] and Katsunori Wakabayashi [1,2,3]

[1] *Department of Nanotechnology for Sustainable Energy, School of Science and Technology, Kwansei Gakuin University, Gakuen-Uegahara 1, Sanda 669-1330, Japan*

[2] *National Institute for Materials Science (NIMS), Namiki 1-1, Tsukuba 305-0044, Japan*

[3] *Center for Spintronics Research Network (CSRN), Osaka University, Toyonaka 560-8531, Japan*

(Received 29 November 2022; revised 6 March 2023; accepted 9 March 2023; published 21 March 2023)

Nonlinear optical (NLO) effect plays a crucial role to engineer optical angular frequency and symmetry of electronic system. Metallic transition-metal dichalcogenides are one of two-dimensional (2D) materials, which have no inversion symmetry for odd-number layers. In particular, odd-number-layered $NbSe_2$ has spin splitting owing to Ising-type spin-orbit coupling. In this paper, we numerically calculate the NLO charge and spin conductivities of $NbSe_2$ based on an effective tight-binding model for several different optical effects, i.e., symmetry manipulation by bicircular light (BCL) and bulk photovoltaic effect (shift and injection currents). Under irradiation of BCL which can control the symmetry of electronic system, the current can be generated even in even-number-layered $NbSe_2$. Also, we find that shift current can be generated for odd-number-layered $NbSe_2$, which is robust against electronic scattering, i.e., topological current. The direction of generated shift current can be switched by altering polarization of light. Our results will serve to design opto-spintronics devices based on 2D materials to manipulate the charge and spin currents and their directions by controlling the polarization of incident light which recasts the symmetry of electronic systems.

DOI: 10.1103/PhysRevB.107.115422

I. INTRODUCTION

Interaction of strong coherent light with matter advanced the field of nonlinear optics, which induces a charge polarization nonlinearly. The emergence of second-order nonlinear optical (NLO) effect has been extensively studied in condensed matter physics and materials science [1–4]. It provides the foundation of laser frequency conversion [5–21] and direct current (DC) photocurrent generation [22–31]. In the NLO process, the crystal symmetry is significant. If a crystal is centrosymmetric, no charge polarization occurs. In a noncentrosymmetric crystal, however, nonlinear charge polarization is induced which can generate DC photocurrent without *p-n* junctions [22–31] and second-harmonic generation (SHG) [5–15].

The transition-metal dichalcogenides (TMDC) with the chemical formula MX_2 (M = Mo, W, Nb, Ta; X = S, Se) are layered materials, which can be easily exfoliated into monolayer due to weak van der Waals forces between layers of TMDC [32–36]. Thus, TMDC forms a new class of atomically thin two-dimensional (2D) electronic systems. For NLO response, the advantage of atomically thin 2D materials such as graphene and TMDC is that the phase-matching conditions between incident light and light-induced electric polarization wave can be ignored because of their extremely smaller thickness than the incident light wavelength [5,37,38]. Thus, in few-layered TMDC the NLO effect mainly depends on the crystal symmetry.

The generation mechanisms for NLO current are dominated by parity symmetry P [28]. Under P conserved, NLO charge and spin currents are absent. On the other hand, for P broken, bulk photovoltaic effect is induced in the system. In general, bulk photovoltaic effect has two contributions: (i) shift current and (ii) injection current [4,28,31,39–41]. (i) Shift current is the photoinduced spontaneous DC, which corresponds to the shift of electrons in real space during the optical excitation of electron. (ii) Injection current is net current for different velocities between electron and hole owing to the population imbalance between them induced by photoexcitation. In the noncentrosymmetric system, the linearly polarized (LP) light irradiation solely induces the charge shift current, however, the incident circularly polarized (CP) light solely induces the charge injection current [28].

Further, bicircular light (BCL) is a useful method to optically engineer the symmetry of electronic systems [42–47]. BCL is the superposition of left-handed CP (LCP) light with the angular frequency $n_1\omega$ and right-handed CP (RCP) light with $n_2\omega$ ($n_1 \neq n_2$), which forms the trajectory of rose curve. It is defined as

$$A_{\mathrm{BCL}}(t) = A_L e^{in_1\omega t} + A_R e^{in_2\omega t - i\theta} + \mathrm{c.c.}, \tag{1}$$

where $A_{L\,(R)}$ is amplitude of LCP (RCP) light and θ is a phase difference between LCP and RCP light. The application of BCL can artificially control the symmetry of electronic system and induce charge polarizations along the directions of leaves of BCL.

In this paper, we theoretically consider the NLO effects on metallic TMDCs. The metallic TMDCs such as $NbSe_2$, NbS_2, $TaSe_2$, and TaS_2 are metallic at room temperature, and successively show the charge density wave (CDW) phase [48,49] and superconducting phase at low temperature [50–56]. In these materials, AB-stacking structure is most stable in nature and has different crystal symmetries for an even and odd

number of layers. Even-number-layered TMDCs have a space group D_{3d}, which respect to inversion and out-of-plane mirror symmetries. However, odd-number-layered TMDCs have a space group D_{3h}, which breaks inversion symmetry. Further, owing to the broken inversion symmetry and a strong atomic spin-orbit coupling (SOC) field such as Nb and Ta atoms, its system possesses Ising-type SOC [52–54,57–60], i.e., an effective Zeeman field that locks electron spins to out-of-plane directions by in-plane momentum.

In $NbSe_2$, the SOC causes large spin splitting in the energy band structures of odd-number-layered systems (about 157 meV at the K point), which leads to unconventional topological spin properties. In actuality, we have shown that monolayer $NbSe_2$ can generate the spin Hall current under visible light irradiation owing to its finite topological spin Berry curvature [61]. Also, we have studied that the second-order NLO charge and spin Hall currents of SHG process can be selectively generated in few-layered $NbSe_2$ according to the crystal symmetry and polarization of incident light [62].

Here, we extend our theoretical analysis to NLO charge and spin conductivities under BCL irradiation and DC photocurrent (shift and injection current) in few-layered $NbSe_2$. We employ the effective tight-binding model (TBM) including the electron hopping among d_{z^2}, d_{xy}, and $d_{x^2-y^2}$ orbitals of Nb atom and Ising-type SOC in order to describe the electronic structures of $NbSe_2$ around the Fermi level. In general, the second-order NLO current is generated in odd-number-layered $NbSe_2$, but absent in even-number-layered $NbSe_2$. However, since BCL can manipulate the symmetry of electronic states, the NLO current can be generated even in even-number-layered $NbSe_2$. In addition, we find that the charge and spin shift currents can be generated in odd-number-layered $NbSe_2$, which is robust to the electronic scattering, i.e., topological current. In addition, the direction of the generated shift current can be switched if LP light is altered to CP light. Our results will serve to design opto-spintronics devices on the basis of 2D materials to manipulate the charge and spin currents and their directions by controlling the polarization of incident light which recasts the crystal symmetry.

This paper is organized as follows. In Sec. II we discuss the crystal symmetry and electronic structures of few-layered $NbSe_2$ based on the effective TBM. In Sec. III we briefly introduce the formula to calculate the second-order NLO conductivities and discuss their relation to the crystal symmetry. In Sec. IV we will show that incident BCL can control the symmetry of the electronic system, which induces the NLO current along the directions of leaves of BCL. In Sec. V we show that the shift current has NLO selection rule depending on the crystal symmetry and polarization of incident light. It is also shown that charge and spin shift currents can be switched if the polarization is altered. Section VI provides the summary of our results. In the Appendix, we give the symmetry analysis on NLO conductivity, NLO current induced by multileaf BCL, and contour plots of integrand of NLO conductivities. In the Supplemental Material, we show the imaginary parts of the NLO conductivities for BCL, rotational angle dependencies of BCL on NLO conductivities, the derivation of shift- and injection-current conductivities, and the NLO conductivity for MoS_2 as a reference of a TMDC semiconductor [63].

II. MODEL

We will show that the second-order NLO charge and spin conductivities strongly depend on the crystal symmetry and the polarization of light in metallic TMDC. In this paper, we employ $NbSe_2$ as an exapmle of metallic TMDCs. Since $NbSe_2$ can be easily exfoliated because of van der Waals forces between layers, few-layered $NbSe_2$ such as monolayer, the AB-stacked bilayer, and ABA-stacked trilayer are obtained. In particular, we focus on two cases which are odd-number layered (e.g., monolayer and ABA-stacked trilayer) and even-number layered (e.g., AB-stacked bilayer) $NbSe_2$. Figure 1(a) shows the side view of few-layered $NbSe_2$. The stacking structure is consisted by inserting the B monolayer (180° rotation of the A monolayer) between A monolayers, which is the most energetically stable stacking sequence in $NbSe_2$. Each layer (monolayer) has the out-of-plane mirror symmetry M_z in perpendicular direction with respect to the plane of Nb atoms. Figures 1(b) and 1(c) show the top views of monolayer and AB-stacked bilayer (ABA-stacked trilayer) $NbSe_2$, respectively. Odd-number-layered $NbSe_2$ has a space group D_{3h}, which has mirror symmetry M_xM_z and no inversion symmetry. On the other hand, in even-number-layered $NbSe_2$, the system has a space group D_{3d}, which respects to two mirror symmetries M_xM_z and M_yM_z and inversion symmetry P. Figure 1(d) shows the first Brillouin zone (BZ) for few-layered $NbSe_2$.

For $NbSe_2$, we employ a multiorbital TBM which includes d_{z^2}, d_{xy}, and $d_{x^2-y^2}$ orbitals of Nb atom, which can well describe the electronic states of $NbSe_2$ around Fermi energy ($E_F = 0$ eV) [52,61,62,64,65]. The eigenvalue equation for the effective TBM is $\hat{H}(\boldsymbol{k})|u_{n\boldsymbol{k}}\rangle = E_{n\boldsymbol{k}}|u_{n\boldsymbol{k}}\rangle$, where n is the band index with spin states expressed as $n = 1, 2, \ldots, 6N$ (N is the number of layer), $\boldsymbol{k} = (k_x, k_y)$ is the wave-number vector for 2D material, and $E_{n\boldsymbol{k}}$ is the eigenvalue for the nth band. The eigenvector for the nth band is defined as $|u_{n\boldsymbol{k}}\rangle = (c_{n\boldsymbol{k},d_{z^2},\uparrow}, c_{n\boldsymbol{k},d_{xy},\uparrow}, c_{n\boldsymbol{k},d_{x^2-y^2},\uparrow}, c_{n\boldsymbol{k},d_{z^2},\downarrow}, c_{n\boldsymbol{k},d_{xy},\downarrow}, c_{n\boldsymbol{k},d_{x^2-y^2},\downarrow})^T$, where $(\ldots)^T$ indicates the transpose of vector and $c_{n\boldsymbol{k}\tau s}$ means the amplitude at atomic orbital τ with spin s for the nth energy band at $\boldsymbol{k}$. The Hamiltonian of monolayer $NbSe_2$ with Ising-type SOC is

$$\hat{H}_{\mathrm{mono}}(\boldsymbol{k}) = \hat{\sigma}_0 \otimes \hat{H}_{\mathrm{TNN}}(\boldsymbol{k}) + \hat{\sigma}_z \otimes \tfrac{1}{2}\lambda_{\mathrm{SOC}}\hat{L}_z \tag{2}$$

with

$$\hat{H}_{\mathrm{TNN}}(\boldsymbol{k}) = \begin{pmatrix} V_0 & V_1 & V_2 \\ V_1^* & V_{11} & V_{12} \\ V_2^* & V_{12}^* & V_{22} \end{pmatrix}, \quad \hat{L}_z = \begin{pmatrix} 0 & 0 & 0 \\ 0 & 0 & -2i \\ 0 & 2i & 0 \end{pmatrix}, \tag{3}$$

where $\hat{\sigma}_0$ and $\hat{\sigma}_z$ are Pauli matrices and λ_{SOC} is the Ising-type SOC parameter ($\lambda_{\mathrm{SOC}} = 0.0784$ eV for monolayer $NbSe_2$). $\hat{H}_{\mathrm{TNN}}(\boldsymbol{k})$ includes the electron hoppings only among three d orbitals of Nb atoms such as d_{z^2}, d_{xy}, and $d_{x^2-y^2}$, which are assumed up to third-nearest-neighbor sites. Similarly, using the Hamiltonian of monolayer $NbSe_2$ $\hat{H}_{\mathrm{mono}}(\boldsymbol{k})$, the Hamiltonians of bilayer and trilayer $NbSe_2$ can be written as

$$\hat{H}_{\mathrm{bi}}(\boldsymbol{k}) = \begin{pmatrix} \hat{H}_{\mathrm{mono}}(-\boldsymbol{k}) & \hat{H}_{\mathrm{int}}(\boldsymbol{k}) \\ \hat{H}_{\mathrm{int}}^{\dagger}(\boldsymbol{k}) & \hat{H}_{\mathrm{mono}}(\boldsymbol{k}) \end{pmatrix} \tag{4}$$

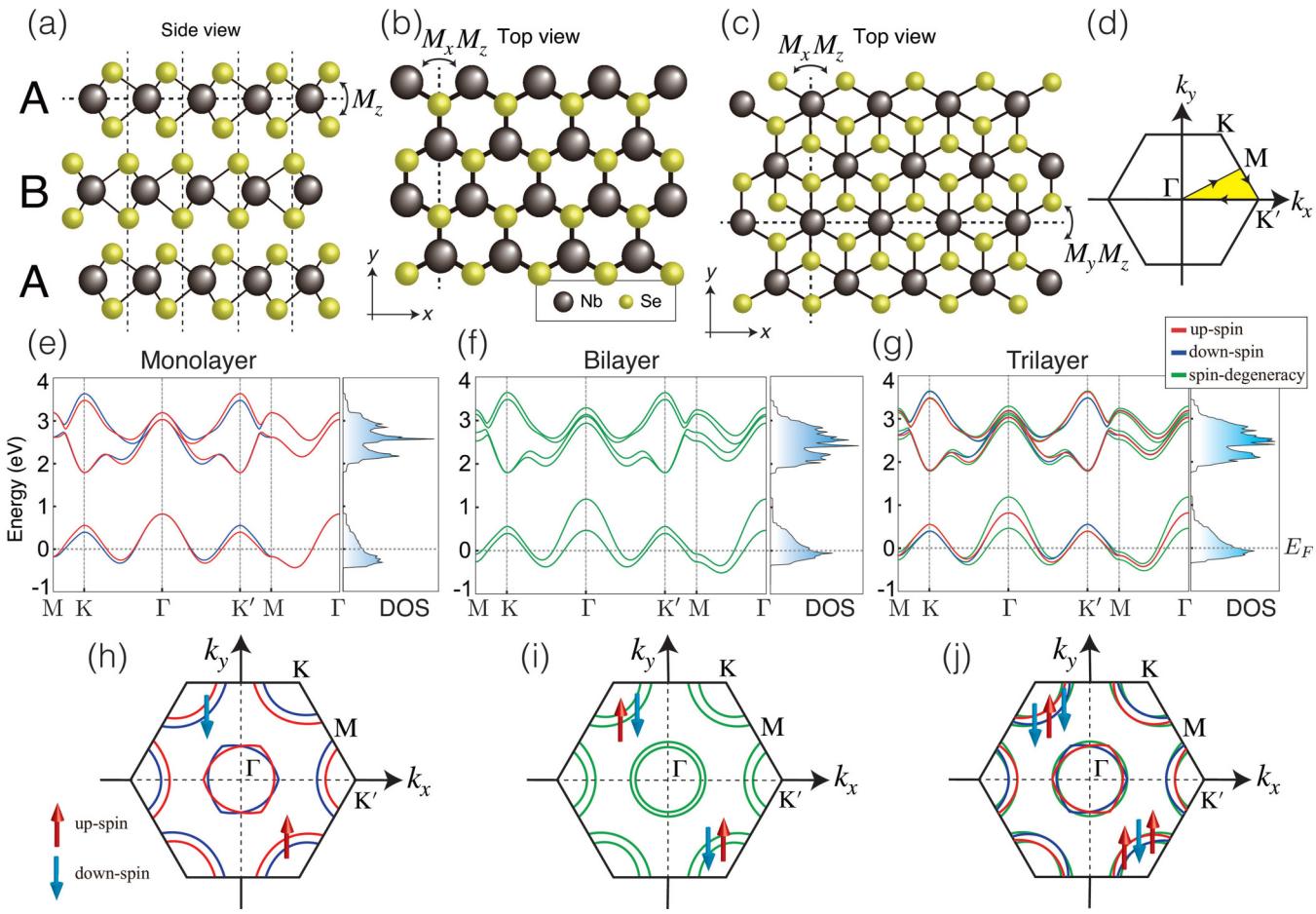

FIG. 1. Crystal structures of few-layered $NbSe_2$ with Nb (black) and Se (yellow) atoms. (a) Side view of crystal structure of monolayer (A), bilayer (AB), and trilayer (ABA) $NbSe_2$. Monolayer $NbSe_2$ has mirror symmetry M_z in perpendicular direction with respect to the plane. Top views of crystal structures of (b) monolayer, (c) bilayer, and trilayer $NbSe_2$, respectively. Odd-number-layered $NbSe_2$ has mirror symmetry M_xM_z and no inversion symmetry, but even-number-layered $NbSe_2$ has inversion symmetry because of mirror symmetries M_xM_z and M_yM_z. (d) First BZ of $NbSe_2$. Energy band structures and DOS of (e) monolayer, (f) bilayer, and (g) trilayer $NbSe_2$ with SOC parameter $\lambda_{SOC} = 0.0784$ eV, respectively. Fermi level is set to zero. Fermi surfaces of (h) monolayer, (i) bilayer, and (j) trilayer $NbSe_2$, respectively. Red, blue, and green lines indicate up-spin, down-spin, and spin-degeneracy states, respectively.

and

$$\hat{H}_{\rm tri}(\boldsymbol{k}) = \begin{pmatrix} \hat{H}_{\rm mono}(\boldsymbol{k}) & \hat{H}_{\rm int}(\boldsymbol{k}) & 0 \\ \hat{H}^{\dagger}_{\rm int}(\boldsymbol{k}) & \hat{H}_{\rm mono}(-\boldsymbol{k}) & \hat{H}_{\rm int}(\boldsymbol{k}) \\ 0 & \hat{H}^{\dagger}_{\rm int}(\boldsymbol{k}) & \hat{H}_{\rm mono}(\boldsymbol{k}) \end{pmatrix}, \quad (5)$$

respectively [54]. Here, the interlayer coupling Hamiltonian $\hat{H}_{\rm int}(\boldsymbol{k})$ between monolayers is

$$\hat{H}_{\rm int}(\boldsymbol{k}) = \begin{pmatrix} T_{01} & 0 & 0 \\ 0 & T_{02} & 0 \\ 0 & 0 & T_{02} \end{pmatrix}. \quad (6)$$

The details of matrix elements V_0, V_1, V_2, V_{11}, V_{12}, V_{22}, T_{01}, and T_{02} can be found in Refs. [61,62].

Figures 1(e)–1(g) show the energy band structures and density of states (DOS) of monolayer, bilayer, and trilayer $NbSe_2$, respectively. Here, red, blue, and green lines indicate up-spin, down-spin, and spin-degeneracy states, respectively. Fermi energy E_F is set to 0 eV. Also, the system has a large energy band gap between the partially filled valence bands and empty conduction bands (about 1.5 eV). Because of the broken inversion symmetry in odd-number-layered $NbSe_2$, the spin-splitting bands can be seen, which show opposite spin states at the valence band edges at K and K' points in the energy band structure, i.e., preservation of time-reversal symmetry. On the other hand, since even-number-layered $NbSe_2$ has crystal inversion symmetry, spin-degeneracy states appear in the energy band structure. In even-number-layered $NbSe_2$, the interlayer interaction has larger effects on the valence band at the Γ point than K and K' points, which leads to the large band splitting of valence band at the Γ point. In trilayer $NbSe_2$, the energy band consists of spin-splitting and spin-degeneracy states. It should be noted that the energy band structure of trilayer $NbSe_2$ can be understood by superposition of monolayer and bilayer $NbSe_2$.

Figures 1(h)–1(j) show the spin-dependent Fermi surfaces of monolayer, bilayer, and trilayer $NbSe_2$, respectively. In odd-number-layered $NbSe_2$, the Fermi surface has up- and down-spin hole pockets centered at Γ, K, and K' points. However, in even-number-layered $NbSe_2$, no such spin splitting occurs owing to the inversion symmetry. Thus, we show that

TABLE I. Second-order NLO charge and spin conductivities of SHG process $\sigma_{ijk}^{\text{charge}}(2\omega;\omega,\omega)$ and $\sigma_{ijk}^{\text{spin}}(2\omega;\omega,\omega)$ for odd- and even-number-layered $NbSe_2$ [62].

	Second-order NLO charge conductivity	Second-order NLO spin conductivity
Odd-number layer (D_{3h})	$\sigma_{yyy}^{\text{charge}} = -\sigma_{yxx}^{\text{charge}} = -\sigma_{xyx}^{\text{charge}} = -\sigma_{xxy}^{\text{charge}}$	$\sigma_{xxx}^{\text{spin}} = -\sigma_{xyy}^{\text{spin}} = -\sigma_{yxy}^{\text{spin}} = -\sigma_{yyx}^{\text{spin}}$
Even-number layer (D_{3d})	Zero	Zero

the spin dependence of Fermi surfaces behaves differently for even- and odd-number-layered $NbSe_2$.

III. SECOND-ORDER NLO CHARGE AND SPIN CONDUCTIVITIES

Under irradiation of light with strong amplitude, the current density J_i can be expanded as follows, i.e., $J_i = J_i^{(1)} + J_i^{(2)} + J_i^{(3)} + \cdots$. Here, $J_i^{(1)}$ is the linear optical current. $J_i^{(2)}$ and $J_i^{(3)}$ are second- and third-order NLO currents. In second-order NLO effect, the generated current density $J_i^{(2)}$ can be given as

$$J_i^{(2)} = \sum_{jk}\sum_{\omega_1\omega_2} \sigma_{ijk}^{(2)}(\omega_1+\omega_2;\omega_1,\omega_2)E_j(\omega_1)E_k(\omega_2), \quad (7)$$

where $E_j(\omega_1)$ and $E_k(\omega_2)$ are electric fields of incident light [3]. Note that (i, j, k) is x or y direction. In particular, i means the generation direction of NLO current. j and k are the polarization of $E_j(\omega_1)$ and $E_k(\omega_2)$. $\sigma_{ijk}^{(2)}(\omega_1+\omega_2;\omega_1,\omega_2)$ is the second-order NLO conductivity. In general, the second-order NLO conductivity is given by the (second-order) Kubo formula [4,8,9,13,15,28,62,66–70]

$$\sigma_{ijk}^{(2)}(\omega_1+\omega_2;\omega_1,\omega_2) \equiv -\frac{\hbar^2 e^2}{2S}\sum_{\boldsymbol{k}}\left[\Omega_{ijk}^{(2)}(\omega_1,\omega_2,\boldsymbol{k}) + \Omega_{ikj}^{(2)}(\omega_2,\omega_1,\boldsymbol{k})\right] \quad (8)$$

with

$$\begin{aligned}\Omega_{ijk}^{(2)}(\omega_1,\omega_2,\boldsymbol{k}) &= \sum_{nml}\frac{j_{mn}^i}{E_{ml}E_{ln}[E_{mn}-\hbar(\omega_1+\omega_2)-i\eta]} \\ &\quad\times\left[\frac{v_{nl}^j v_{lm}^k f_{ml}}{E_{ml}-\hbar\omega_2-i\eta} - \frac{v_{nl}^k v_{lm}^j f_{ln}}{E_{ln}-\hbar\omega_2-i\eta}\right] \\ &= \sum_{nml}\frac{f_{lm}v_{lm}^k}{E_{ml}(E_{ml}-\hbar\omega_2-i\eta)} \\ &\quad\times\left[\frac{j_{mn}^i v_{nl}^j}{E_{nl}[E_{mn}-\hbar(\omega_1+\omega_2)-i\eta]}\right. \\ &\quad\left. - \frac{v_{mn}^j j_{nl}^i}{E_{mn}[E_{nl}-\hbar(\omega_1+\omega_2)-i\eta]}\right], \end{aligned} \quad (9)$$

which describes the contribution of the interband optical transition [71]. $\Omega_{ijk}^{(2)}(\omega_1,\omega_2,\boldsymbol{k})$ is the integrand of $\sigma_{ijk}^{(2)}(\omega_1+\omega_2;\omega_1,\omega_2)$ before considering intrinsic permutation symmetry, i.e., $\Omega_{ijk}^{(2)}(\omega_1,\omega_2,\boldsymbol{k}) = \Omega_{ikj}^{(2)}(\omega_2,\omega_1,\boldsymbol{k})$. Note that (n, m, l) are the band indices including spin degree of freedom. $v_{nl}^j = \langle u_{n\boldsymbol{k}}|\boldsymbol{v}\cdot\boldsymbol{e_j}|u_{l\boldsymbol{k}}\rangle$, and $\boldsymbol{v}$ is the group velocity operator, which is written as $\boldsymbol{v} = (\hat{v}_x, \hat{v}_y) = \frac{1}{\hbar}(\frac{\partial\hat{H}}{\partial k_x}, \frac{\partial\hat{H}}{\partial k_y})$ for 2D materials. $\boldsymbol{e_j}$ ($\boldsymbol{e_k}$) is the Jones vector. For example, $\boldsymbol{e_x} = (1,0)^T$ for x-polarized light, $\boldsymbol{e_y} = (0,1)^T$ for y-polarized light, $\boldsymbol{e_L} = \frac{1}{\sqrt{2}}(1,i)^T$ for LCP light, and $\boldsymbol{e_R} = \frac{1}{\sqrt{2}}(1,-i)^T$ for RCP light. $|u_{n\boldsymbol{k}}\rangle$ is the eigenfunction with the eigenenergy $E_{n\boldsymbol{k}}$ and $f(E_{n\boldsymbol{k}})$ is the Fermi-Dirac distribution function. E_{ml} is the difference between energy levels $E_{m\boldsymbol{k}}$ and $E_{l\boldsymbol{k}}$, i.e., $E_{ml} \equiv E_{m\boldsymbol{k}} - E_{l\boldsymbol{k}}$, and f_{ml} is also defined as $f_{ml} \equiv f(E_{m\boldsymbol{k}}) - f(E_{l\boldsymbol{k}})$. ω_1 and ω_2 are optical angular frequencies for the absorption process. η is an infinitesimally small real number and S is the area of 2D system. Throughout this paper, $\eta = 0.001$ eV is set for the calculation of conductivity. $j_{mn}^i = \langle u_{m\boldsymbol{k}}|\hat{j}_i^{(2)}|u_{n\boldsymbol{k}}\rangle$, where $\hat{j}_i^{(2)}$ is current density operator, and represented as $\hat{j}_i^{\text{charge}} = \frac{1}{2}\{-e\hat{\sigma}_0\otimes\hat{I}_N, \hat{v}_i\}$ for charge current and $\hat{j}_i^{\text{spin}} = \frac{1}{2}\{\frac{\hbar}{2}\hat{\sigma}_z\otimes\hat{I}_N, \hat{v}_i\}$ for spin current. Here, $\hat{I}_N$ is the $N\times N$ identity matrix and in particular $N = 3, 6, 9$ is used for monolayer, bilayer, and trilayer $NbSe_2$, respectively.

In Eqs. (8) and (9), when $\omega_1+\omega_2 = \omega_3$ and $\omega_1 \neq \omega_2 \neq \omega_3 \neq 0$, the process is called as sum frequency generation (SFG) [16–18]. In particular, if $\omega_1 = \omega_2 \equiv \omega \neq 0$ and $\omega_3 = 2\omega$, the process becomes SHG. In addition, when $\omega_1 - \omega_2 = \omega_3$ and $\omega_1 \neq \omega_2 \neq \omega_3 \neq 0$, the process is called as difference frequency generation (DFG) [72,73], which can express the bulk photovoltaic effect if $\omega_1 = -\omega_2 \equiv \omega \neq 0$.

The NLO conductivities are strongly influenced by the crystal symmetries [3]. For the SHG process in the odd-number-layered $NbSe_2$ where the inversion symmetry is broken, the NLO charge and spin conductivities of the SHG process $\sigma_{ijk}^{\text{charge}}(2\omega;\omega,\omega)$ and $\sigma_{ijk}^{\text{spin}}(2\omega;\omega,\omega)$ have the following relations:

$$\begin{aligned}\sigma_{yyy}^{\text{charge}}(2\omega;\omega,\omega) &= -\sigma_{yxx}^{\text{charge}}(2\omega;\omega,\omega) \\ &= -\sigma_{xyx}^{\text{charge}}(2\omega;\omega,\omega) = -\sigma_{xxy}^{\text{charge}}(2\omega;\omega,\omega)\end{aligned} \quad (10)$$

and

$$\begin{aligned}\sigma_{xxx}^{\text{spin}}(2\omega;\omega,\omega) &= -\sigma_{xyy}^{\text{spin}}(2\omega;\omega,\omega) \\ &= -\sigma_{yxy}^{\text{spin}}(2\omega;\omega,\omega) = -\sigma_{yyx}^{\text{spin}}(2\omega;\omega,\omega).\end{aligned} \quad (11)$$

The other elements are absent. On the other hand, in even-number-layered $NbSe_2$, the NLO current is always absent owing to the inversion symmetry. These results are summarized in Table I. In addtion, another derivation of these relations using crystal symmetry operation is presented in Appendix A.

IV. NLO CONDUCTIVITY UNDER IRRADIATION OF BCL

BCL can artificially control the symmetry of electronic system [42–47,74–76]. BCL is the superposition of LCP and

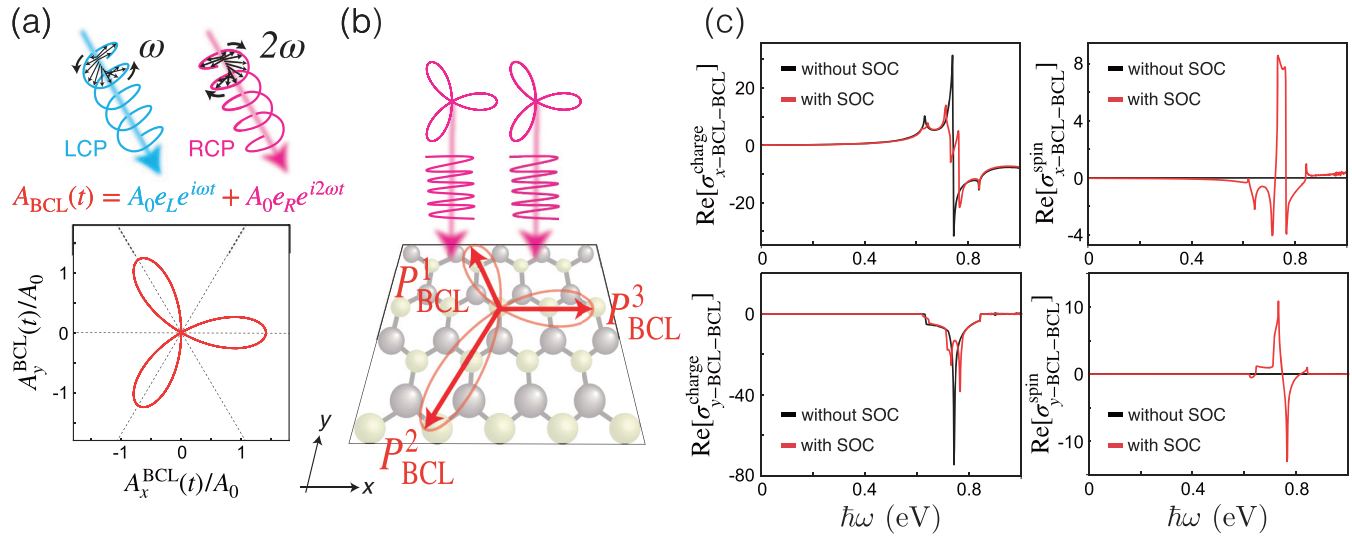

FIG. 2. (a) Trajectory of three-leaf BCL ($n_1 : n_2 = 1 : 2, \theta = 0$). (b) Schematic of three induced polarizations $P^1_{\rm BCL}$, $P^2_{\rm BCL}$, and $P^3_{\rm BCL}$ by irradiating three-leaf BCL. (c) Real parts of second-order NLO conductivities $\sigma^{\rm charge}_{x\text{-BCL-BCL}}(n_1\omega, n_2\omega)$, $\sigma^{\rm charge}_{y\text{-BCL-BCL}}(n_1\omega, n_2\omega)$, $\sigma^{\rm spin}_{x\text{-BCL-BCL}}(n_1\omega, n_2\omega)$, and $\sigma^{\rm spin}_{y\text{-BCL-BCL}}(n_1\omega, n_2\omega)$ for monolayer $NbSe_2$ under irradiation of BCL with three leaves. Black and red lines indicate the NLO conductivities without and with SOC. The units of $\sigma^{\rm charge}_{i\text{-BCL-BCL}}(n_1\omega, n_2\omega)$ and $\sigma^{\rm spin}_{i\text{-BCL-BCL}}(n_1\omega, n_2\omega)$ are $e^3/\hbar$ and e^2, respectively.

RCP light with different angular frequencies $n_1\omega$ and $n_2\omega$, where n_1 and n_2 are different integers. The vector potential for BCL can be formulated as

$$\begin{aligned} A(t) &= A_L e^{in_1\omega t} + A_R e^{in_2\omega t - i\theta} + \text{c.c.} \\ &= \frac{1}{\sqrt{2}}(A_x + iA_y)e^{in_1\omega t} + \frac{1}{\sqrt{2}}(A_x - iA_y)e^{in_2\omega t - i\theta} + \text{c.c.}, \end{aligned} \tag{12}$$

where $A_{L\,(R)}$ is the amplitude of the LCP (RCP) light. θ is the phase difference between LCP and RCP light. In general, the trajectory of BCL is a rose curve with $(n_1 + n_2)/\gcd(n_1, n_2)$-fold rotation symmetry. Here, $\gcd(n_1, n_2)$ means the great common divisor of two integers n_1, n_2. For example, there are three-leaf BCL with threefold rotation symmetry C_3, four-leaf BCL with fourfold rotation symmetry C_4, and five-leaf BCL with fivefold rotation symmetry C_5.

The induced current density $J_i^{\rm BCL}$ under the irradiation of BCL, i.e., $E_{\rm BCL}(t) = E_L e^{in_1\omega t} + E_R e^{in_2\omega t} + \text{c.c.} = \sum_{a=L,R}\sum_{n_a} E_a e^{in_a\omega t}$ with $(n_L, n_R) \equiv (n_1, n_2)$, can be written as

$$J_i^{\rm BCL} = \sum_{ab}\sum_{n_a n_b} \sigma^{(2)}_{iab}[(n_a + n_b)\omega; n_a\omega, n_b\omega]E_a E_b.$$

Furthermore, the NLO conductivity for BCL irradiation becomes

$$\begin{aligned} &\sigma^{(2)}_{i\text{-BCL-BCL}}(n_1\omega, n_2\omega) \\ &= \sum_{ab} \sigma^{(2)}_{iab}[(n_a + n_b)\omega; n_a\omega, n_b\omega] \\ &= \sigma^{(2)}_{iLL}(2n_1\omega; n_1\omega, n_1\omega) + \sigma^{(2)}_{iLR}[(n_1 + n_2)\omega; n_1\omega, n_2\omega] \\ &\quad + \sigma^{(2)}_{iRL}[(n_2 + n_1)\omega; n_2\omega, n_1\omega] + \sigma^{(2)}_{iRR}(2n_2\omega; n_2\omega, n_2\omega), \end{aligned} \tag{13}$$

where the subscripts BCL and L (R) mean the injection of BCL and LCP (RCP), respectively. The NLO conductivities are numerically calculated by using Eqs. (8) and (9). Figure 2(a) shows the trajectory of incident BCL with three-leaf ($n_1 : n_2 = 1 : 2, \theta = 0$). The three-leaf BCL can break the mirror symmetry M_x and then induce three polarizations $P^1_{\rm BCL}$, $P^2_{\rm BCL}$, and $P^3_{\rm BCL}$ along the directions of three leaves of three-leaf BCL [see Fig. 2(b)]. Figure 2(c) shows the ω dependence of the real parts of second-order NLO conductivities $\sigma^{(2)}_{i\text{-BCL-BCL}}(n_1\omega, n_2\omega)$ for monolayer $NbSe_2$ under irradiation of three-leaf BCL. In previous work, we have shown that under LP light irradiation, the charge and spin Hall current can be generated only either in the y or x direction for monolayer $NbSe_2$ [62]. However, since the three-leaf BCL breaks M_x symmetry, the current can be generated in both x and y directions.

Figure 3(a) shows the trajectory of three-leaf BCL with rotational angle α ($n_1 : n_2 = 1 : 2, \alpha \neq 0$). Here, α has a following relation with θ:

$$\alpha = -\frac{n_1}{n_1 + n_2}\theta, \tag{14}$$

which is defined as rotational angle from the x axis. Figure 3(b) shows α dependence on real parts of second-order NLO conductivities $\sigma^{(2)}_{i\text{-BCL-BCL}}(n_1\omega, n_2\omega)$ for monolayer $NbSe_2$ under irradiation of three-leaf BCL of $\hbar\omega = 2.5$ eV. The charge current is generated along the three different axes of the induced polarizations by incident BCL of three leaves, resulting in the appearance of six equivalent peaks for α ($0 \leqslant \alpha < 2\pi$). On the other hand, the magnitude of spin current has only three equivalent peaks. As shown in the Supplemental Material [63], the NLO conductivities for up- and down-spin states have three equivalent peaks, but point in opposite directions to each other. In general, the number of generated directions of charge and spin currents are twice as different.

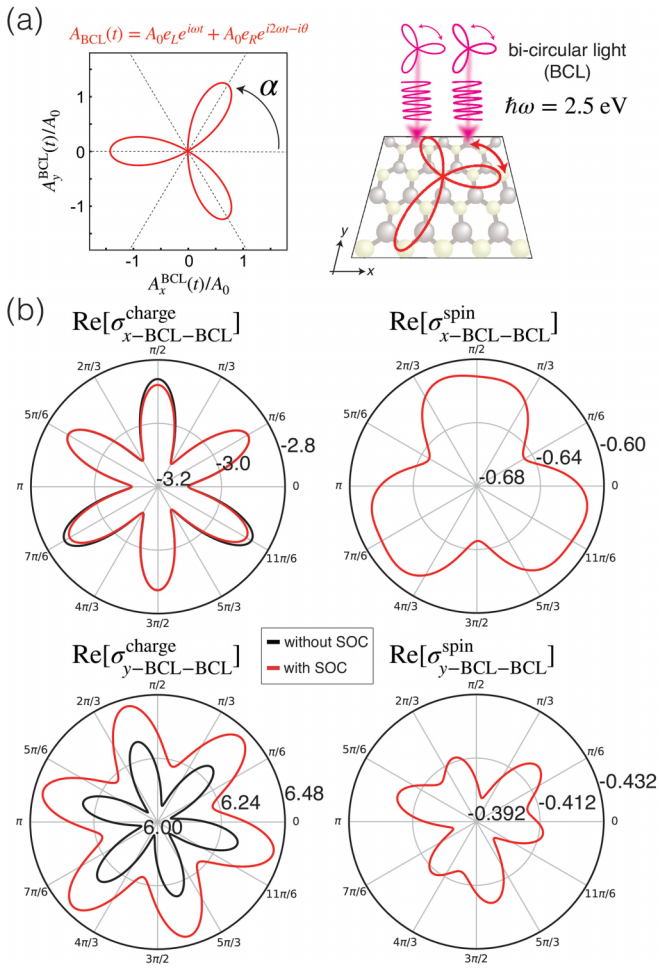

FIG. 3. (a) Trajectory of three-leaf BCL with rotational angle α ($n_1 : n_2 = 1 : 2$, $\alpha \neq 0$). (b) α dependence on real parts of second-order NLO charge and spin conductivities for monolayer $NbSe_2$ under irradiation of three-leaf BCL of $\hbar\omega = 2.5$ eV. Black and red lines indicate $\sigma^{(2)}_{i\text{-BCL-BCL}}(n_1\omega, n_2\omega)$ without and with SOC. The units of $\sigma^{\rm charge}_{i\text{-BCL-BCL}}(n_1\omega, n_2\omega)$ and $\sigma^{\rm spin}_{i\text{-BCL-BCL}}(n_1\omega, n_2\omega)$ are $e^3/\hbar$ and e^2, respectively.

In Appendix A, we derive the selection rules of second-order NLO conductivities of $NbSe_2$ under irradiation of generic BCL. In Appendix B, we provide the second-order NLO conductivities of monolayer $NbSe_2$ for the irradiation of BCL with four, five, six, and seven leaves. As shown in Fig. 8 of Appendix B, it is found that the peaks of NLO conductivities in the range of $0 < \hbar\omega < 1$ shift lower with increase of leaves of BCL. These shifts are originated from the factor of $(n_1 + n_2)$ in the denominator of Eq. (9).

If $n_1 : n_2 = 1 : 1$ with $\theta = 0$, the trajectory of incident light is identical to x-polarized light, i.e.,

$$A_{\rm BCL}(t) = A_L e^{i\omega t} + A_R e^{i\omega t} + \text{c.c.} = \sqrt{2} A_x e^{i\omega t} + \text{c.c.} \quad (15)$$

Therefore, this case reproduces the results of SHG process [62]. The details are shown in the Supplemental Material [63].

In even-number-layered $NbSe_2$, the second-order NLO current is always absent because of the inversion symmetry [62]. However, the irradiation of BCL with odd number of leaves or even number of leaves with $\alpha \neq 0$ can break the inversion symmetry, resulting in the generation of charge and spin currents. As shown in Appendix C, for irradiation of RCP and LCP light with different optical angular frequencies, the NLO current is generated, i.e., no cancellation of current even in the presence of spatial inversion symmetry. Figure 4(a) shows the real parts of $\sigma^{(2)}_{i\text{-BCL-BCL}}(n_1\omega, n_2\omega)$ for bilayer $NbSe_2$ under irradiation of three-leaf BCL. Owing to the broken mirror symmetry M_x, the NLO charge and spin currents can be generated only either in the x or y direction for bilayer $NbSe_2$. Thus, the irradiation of BCL can generate the current even in even-number-layered $NbSe_2$.

In addition, we should notice that in an energy range of $0 < \hbar\omega < 0.1$, $\mathrm{Re}[\sigma^{\rm charge}_{x\text{-BCL-BCL}}]$ and $\mathrm{Re}[\sigma^{\rm spin}_{y\text{-BCL-BCL}}]$ have the peaks for bilayer $NbSe_2$. These peaks are attributed to interband optical transition between highest valence and lowest conduction bands of energy bands shown in Fig. 4(b), which cause infrared light absorption. On the other hand, the infrared light absorption is absent in semiconductor TMDC such as MoS_2 because of the large band gap between valence and conduction bands ($\Delta E \approx 2.0$ eV).

Figure 4(c) schematically summarizes the induced charge and spin current directions in bilayer $NbSe_2$ under irradiation of three-leaf BCL. Since BCL breaks the inversion symmetry of electronic system, the NLO current is generated even in bilayer $NbSe_2$. Note that the charge current is induced along $P^3_{\rm BCL}$ in Fig. 2(b), but the spin current is induced in perpendicular to the charge current.

In Appendix D, we provide the second-order NLO conductivities for trilayer $NbSe_2$ under BCL irradiation. The second-order NLO conductivities of trilayer $NbSe_2$ consist of three optical transition processes: (i) intralayer optical transition of monolayer $NbSe_2$, (ii) intralayer and interlayer optical transition of bilayer $NbSe_2$, and (iii) interlayer optical transitions between monolayer and bilayer $NbSe_2$. Under irradiation of LP light, the process (ii) is absent. However, BCL of three leaves makes all three processes finite.

V. SHIFT- AND INJECTION-CURRENT CONDUCTIVITIES

DFG with $\omega_1 = -\omega_2 \equiv \omega \neq 0$ induces the DC photocurrent, i.e., bulk photovoltaic effect. In Eq. (7), the DC photocurrent $J^{(2)}_i$ can be obtained as

$$\begin{aligned} J^{(2)}_i &= \sum_{jk} \left\{ \sigma^{(2)}_{ijk}(0; \omega, -\omega) E_j(\omega) E_k(-\omega) \right. \\ &\quad \left. + \sigma^{(2)}_{ijk}(0; -\omega, \omega) E_j(-\omega) E_k(\omega) \right\} \\ &= \sum_{jk} \left\{ \sigma^{(2)}_{ijk}(0; \omega, -\omega) E_j(\omega) E_k(-\omega) + \text{c.c.} \right\} \\ &= \sum_{jk} 2\sigma^{(2)}_{ijk}(0; \omega, -\omega) E_j(\omega) E_k(-\omega), \end{aligned} \quad (16)$$

where the DC photoconductivity based on Eqs. (8) and (9) follows the identities $\sigma^{(2)}_{ijk}(0; -\omega, \omega) = -\sigma^{(2)}_{ijk}(0; \omega, -\omega) = [\sigma^{(2)}_{ijk}(0; \omega, -\omega)]^*$. The numerical results are shown in the Supplemental Material [63], which strongly depends on the crystal symmetry, i.e., generation of current for odd-number-layered $NbSe_2$, but absence for even-number-layered $NbSe_2$.

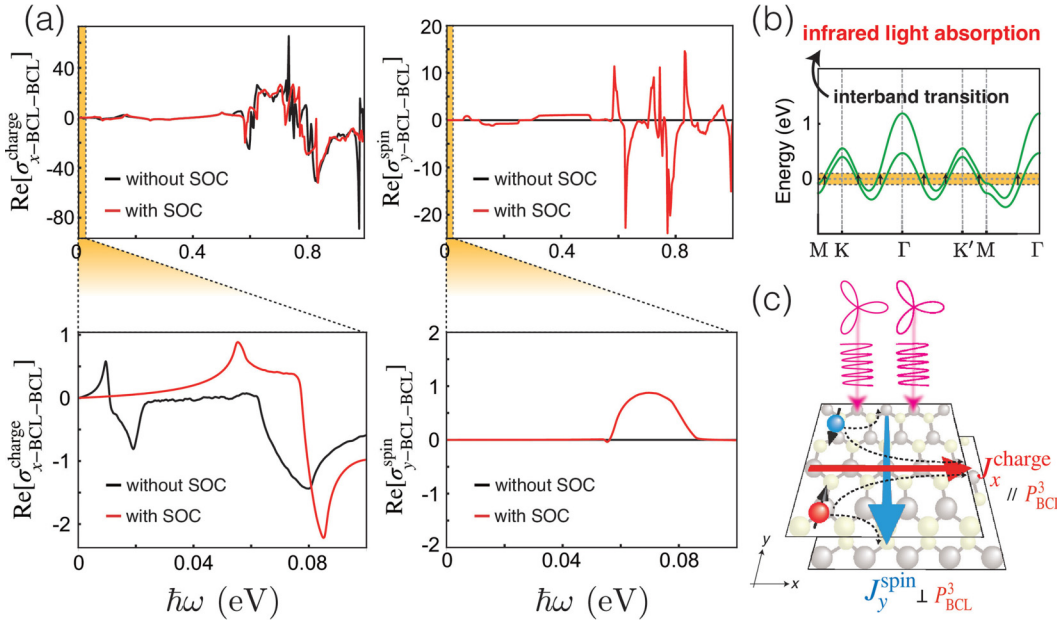

FIG. 4. (a) Real parts of second-order NLO conductivities $\sigma^{\text{charge}}_{x\text{-BCL-BCL}}(n_1\omega, n_2\omega)$ and $\sigma^{\text{spin}}_{y\text{-BCL-BCL}}(n_1\omega, n_2\omega)$ for bilayer $NbSe_2$ under irradiation of BCL with three leaves. In an energy range of $0 < \hbar\omega < 0.1$, the charge and spin conductivities have peaks. (b) Its peaks correspond to infrared light absorption for optical interband transition in energy band of bilayer $NbSe_2$. (c) Schematics of generated charge and spin current by irradiating BCL with three leaves. Black and red lines indicate $\sigma^{(2)}_{i\text{-BCL-BCL}}(n_1\omega, n_2\omega)$ without and with SOC. The units of $\sigma^{\text{charge}}_{i\text{-BCL-BCL}}(n_1\omega, n_2\omega)$ and $\sigma^{\text{spin}}_{i\text{-BCL-BCL}}(n_1\omega, n_2\omega)$ are $e^3/\hbar$ and e^2, respectively.

The bulk photovoltaic effect includes the generation of shift and injection currents. In this section, we derive the shift-and injection-current conductivities, and find that these conductivities depend on the crystal symmetry and polarization of incident light for monolayer $NbSe_2$.

A. Shift and injection currents under LP light irradiation

The DC photocurrent can be separated into two different optically induced DC currents, i.e., (i) shift current and (ii) injection current. (i) Shift current is induced polarization current owing to the shift of electron position by irradiating light [28]. The induced polarization of electrons P_i is written as

$$P_i = e\int_{\text{BZ}} \frac{d\boldsymbol{k}}{(2\pi)^3}\sum_m f_m \xi^i_{mm}, \tag{17}$$

where ξ^i_{mm} is the Berry connection of mth band and $\xi^i_{mm} = i\langle u_{m\boldsymbol{k}}|\frac{\partial}{\partial k_i}|u_{m\boldsymbol{k}}\rangle$ [4]. Berry connection is also interpreted as the Wannier center of wave function [77–79]. Thus, the origin of the shift current is the change of the polarization P_i, i.e., the Berry connection difference between valence and conduction bands $\xi^i_{mm} - \xi^i_{ll}$ by photoexcitation. Note that l (m) is the unoccupied (occupied) band index. (ii) Injection current is induced net current for the distribution of asymmetric electron and hole velocities $\Delta^i_{lm} = v^i_{ll} - v^i_{mm}$ owing to the population imbalance by photoexcitation in the momentum space [28].

Using a sum rule for the generalized derivative $r^j_{ml;i}$ of position $r^j_{ml} = \langle u_{m\boldsymbol{k}}|\boldsymbol{r}\cdot\boldsymbol{e}_j|u_{l\boldsymbol{k}}\rangle$ in the DC photoconductivity $\sigma^{(2)}_{ijk}(0;\omega,-\omega)$ [4,28,39–41], the DC photoconductivity can be separated into shift- and injection-current conductivities. Here, $r^j_{ml;i}$ is given as

$$\begin{aligned} r^j_{ml;i} &= \frac{\partial r^j_{ml}}{\partial k_i} - i\left[\xi^i_{mm} - \xi^i_{ll}\right]r^j_{ml} \\ &= -iR^i_{ml}(\boldsymbol{k})r^j_{ml}, \end{aligned} \tag{18}$$

which depends on the difference of Berry connections, i.e., contribution for shift current. Note that $R^i_{ml}(\boldsymbol{k})$ is shift vector and given as

$$R^i_{ml}(\boldsymbol{k}) = \frac{\partial\phi^j_{ml}}{\partial k_i} + \left(\xi^i_{mm} - \xi^i_{ll}\right), \tag{19}$$

where ϕ^j_{ml} is phase of group velocity $v^j_{ml} = \langle u_{m\boldsymbol{k}}|\boldsymbol{v}\cdot\boldsymbol{e}_j|u_{l\boldsymbol{k}}\rangle = |v^j_{ml}|e^{-i\phi^j_{ml}}$. For the numerical calculation, it is better to rewrite the generalized derivative $r^j_{ml;i}$ as follows:

$$\begin{aligned} r^j_{ml;i} &= \frac{r^i_{ml}\Delta^j_{lm} + r^j_{ml}\Delta^i_{lm}}{\omega_{ml}} \\ &\quad - i\hbar^2\sum_{n\neq m,l}\left(\frac{v^i_{mn}v^j_{nl}}{E_{ml}E_{mn}} - \frac{v^j_{mn}v^i_{nl}}{E_{ml}E_{nl}}\right). \end{aligned} \tag{20}$$

Using the relation of r^i_{ml} and v^i_{ml} for interband optical transition, i.e.,

$$r^i_{ml} = \begin{cases} \frac{v^i_{ml}}{i\omega_{ml}} & (m\neq l), \\ 0 & (m = l), \end{cases} \tag{21}$$

Eq. (20) is rewritten as the expression with velocity. Thus, $r^j_{ml;i}$ becomes

$$\begin{aligned} r^j_{ml;i} &= -\hbar R^i_{ml}(\boldsymbol{k})\frac{v^j_{ml}}{E_{ml}} \\ &= -\frac{2i\hbar^2}{E_{ml}}\left[\frac{v^i_{ml}\left(v^j_{ll}-v^j_{mm}\right)}{E_{ml}}+\frac{v^j_{ml}\left(v^i_{ll}-v^i_{mm}\right)}{E_{ml}}\right. \\ &\quad \left.+\sum_n\left(\frac{v^i_{mn}v^j_{nl}}{E_{mn}}-\frac{v^j_{mn}v^i_{nl}}{E_{nl}}\right)\right], \end{aligned} \tag{22}$$

where v^i_{ml} is $\langle u_{m\boldsymbol{k}}|\hat{j}^{\text{charge}}_i|u_{l\boldsymbol{k}}\rangle = \frac{1}{2}\langle u_{m\boldsymbol{k}}|\{-e\hat{\sigma}_0\otimes\hat{I}_N,\hat{v}_i\}|u_{l\boldsymbol{k}}\rangle$ for charge current and $\langle u_{m\boldsymbol{k}}|\hat{j}^{\text{spin}}_i|u_{l\boldsymbol{k}}\rangle = \frac{1}{2}\langle u_{m\boldsymbol{k}}|\{\frac{\hbar}{2}\hat{\sigma}_z\otimes\hat{I}_N,\hat{v}_i\}|u_{l\boldsymbol{k}}\rangle$ for spin current. Thus, by substituting the second term of Eq. (22) in the summation part of Eq. (9) with $\omega_1=-\omega_2\equiv\omega\neq 0$, the DC photoconductivity becomes $\sigma^{(2)}_{ijk}(0;\omega,-\omega)=\sigma^{\text{shift}}_{ijk}(0;\omega,-\omega)+\sigma^{\text{injection}}_{ijk}(0;\omega,-\omega)$. Here, $\sigma^{\text{shift}}_{ijk}(0;\omega,-\omega)$ are the shift-current and $\sigma^{\text{injection}}_{ijk}(0;\omega,-\omega)$ are injection-current conductivities.

For LP light irradiation, $\sigma^{\text{shift}}_{ijk}(0;\omega,-\omega)$ and $\sigma^{\text{injection}}_{ijk}\times(0;\omega,-\omega)$ are derived as [39]

$$\sigma^{\text{shift}}_{ijk}(0;\omega,-\omega)=-\frac{i\hbar e^3}{S}\sum_{\boldsymbol{k}}\sum_{mn}f_{nm}\frac{\alpha^{jk}_{mn}(\boldsymbol{k})R^i_{nm}(\boldsymbol{k})}{E^2_{mn}(E_{mn}-\hbar\omega-i\eta)} \tag{23}$$

with transition intensity

$$\alpha^{jk}_{mn}(\boldsymbol{k})=\tfrac{1}{2}\left[v^j_{mn}(\boldsymbol{k})v^k_{nm}(\boldsymbol{k})+v^k_{mn}(\boldsymbol{k})v^j_{nm}(\boldsymbol{k})\right] \tag{24}$$

and

$$\sigma^{\text{injection}}_{ijk}(0;\omega,-\omega)=\tau\frac{i\hbar e^3}{S}\sum_{\boldsymbol{k}}\sum_{mn}f_{nm}\frac{\alpha^{jk}_{mn}(\boldsymbol{k})\Delta^i_{mn}(\boldsymbol{k})}{E^2_{mn}(E_{mn}-\hbar\omega-i\eta)}, \tag{25}$$

where the dummy variables $(m\to n, l\to m)$ are interchanged and $\tau=\hbar/\eta$. For spin current, the superscripts of these conductivities are rewritten as "spin shift" and "spin injection." It should be noted that the spin-dependent position and velocity difference for the direction of generated current are $r^j_{ml;i(\text{spin})}$ and $\Delta^{i\,\text{spin}}_{lm}$. According to Ref. [28], since these approaches of length [4] and velocity gauges [39] should be equivalent, we use the expression of velocity gauge for our calculation.

Since the shift current strongly depends on the crystal symmetry, the charge and spin shift currents can be generated in odd-number-layered $NbSe_2$, but absent in even-number-layered $NbSe_2$. The finite charge and spin-shift-current conductivities can be obtained as

$$\begin{aligned} \sigma^{\text{shift}}_{yyy}(0;\omega,-\omega) &= -\sigma^{\text{shift}}_{yxx}(0;\omega,-\omega) \\ &= -\sigma^{\text{shift}}_{xyx}(0;\omega,-\omega)=-\sigma^{\text{shift}}_{xxy}(0;\omega,-\omega) \end{aligned} \tag{26}$$

and

$$\begin{aligned} \sigma^{\text{spin shift}}_{xxx}(0;\omega,-\omega) &= -\sigma^{\text{spin shift}}_{xyy}(0;\omega,-\omega) \\ &= -\sigma^{\text{spin shift}}_{yxy}(0;\omega,-\omega) \\ &= -\sigma^{\text{spin shift}}_{yyx}(0;\omega,-\omega), \end{aligned} \tag{27}$$

respectively. The other elements are absent for monolayer $NbSe_2$. These relations are equivalent to the results of the SHG process [62].

Figure 5(a) shows the charge and spin-shift-current conductivities for monolayer $NbSe_2$ under irradiation of LP light. Because of the broken inversion symmetry, the charge and spin shift currents can be generated in the y and x directions for linearly x-polarized light, respectively. On the other hand, for linearly y-polarized light, the charge and spin shift currents can be generated in the y and x directions, respectively. We should note that the generated spin shift current is perpendicular to the charge current.

The appearance of charge (spin) shift current along y (x) direction can also be understood by inspecting $\alpha^{jk}_{mn}(\boldsymbol{k})$ with $jk=xx,yy$ and $R^i_{nm}(\boldsymbol{k})$, which are contained in the integrand of Eq. (23). When the product $\alpha^{jk}_{mn}(\boldsymbol{k})R^i_{nm}(\boldsymbol{k})$ with $jk=xx,yy$ is even with respect to π rotation, we obtain the finite charge (spin) shift current along the y (x) direction. The contour plots of $\alpha^{jk}_{mn}(\boldsymbol{k})$ and $R^i_{nm}(\boldsymbol{k})$ can be found in Fig. 11 in Appendix E. Since $\alpha^{jk}_{mn}(\boldsymbol{k})$ with $jk=xx,yy$ is even for π rotation, the shift current is absent for $R^i_{mm}(\boldsymbol{k})$ with odd parity. On the other hand, the finite elements of injection-current conductivities have the following relation:

$$\begin{aligned} \sigma^{\text{spin injection}}_{xxx}(0;\omega,-\omega) &= -\sigma^{\text{spin injection}}_{xyy}(0;\omega,-\omega) \\ &= -\sigma^{\text{spin injection}}_{yxy}(0;\omega,-\omega) \\ &= -\sigma^{\text{spin injection}}_{yyx}(0;\omega,-\omega), \end{aligned} \tag{28}$$

however, the other elements are absent for monolayer $NbSe_2$.

Figure 5(b) shows the spin injection-current conductivities for monolayer $NbSe_2$ under LP light irradiation. Owing to the broken inversion symmetry, the spin injection current can be generated in the x direction for x and y polarized light. As shown in Fig. 5(c), the magnitude of the generated spin injection current is larger than that of spin shift current owing to τ dependence of injection current. Here, the plots of conductivities are shown in logarithmic scale. Thus, if τ increases, the magnitude of injection current becomes larger, but that of shift current is robust, i.e., topologically protected.

We also find that the parity of $\alpha^{jk}_{mn}(\boldsymbol{k})\Delta^i_{mn}(\boldsymbol{k})$ in the integrand of Eq. (25) is involved in the generation of injection current. As shown in Fig. 11 in Appendix E, $\alpha^{jk}_{mn}(\boldsymbol{k})$ with $jk=xx,yy$ and $\Delta^{x-\text{spin}}_{mn}(\boldsymbol{k})$ are even for π rotation. Thus, the spin injection current is generated in the x direction, because $\alpha^{jk}_{mn}(\boldsymbol{k})\Delta^i_{mn}(\boldsymbol{k})$ with $jk=xx,yy$ is even with respect to π rotation.

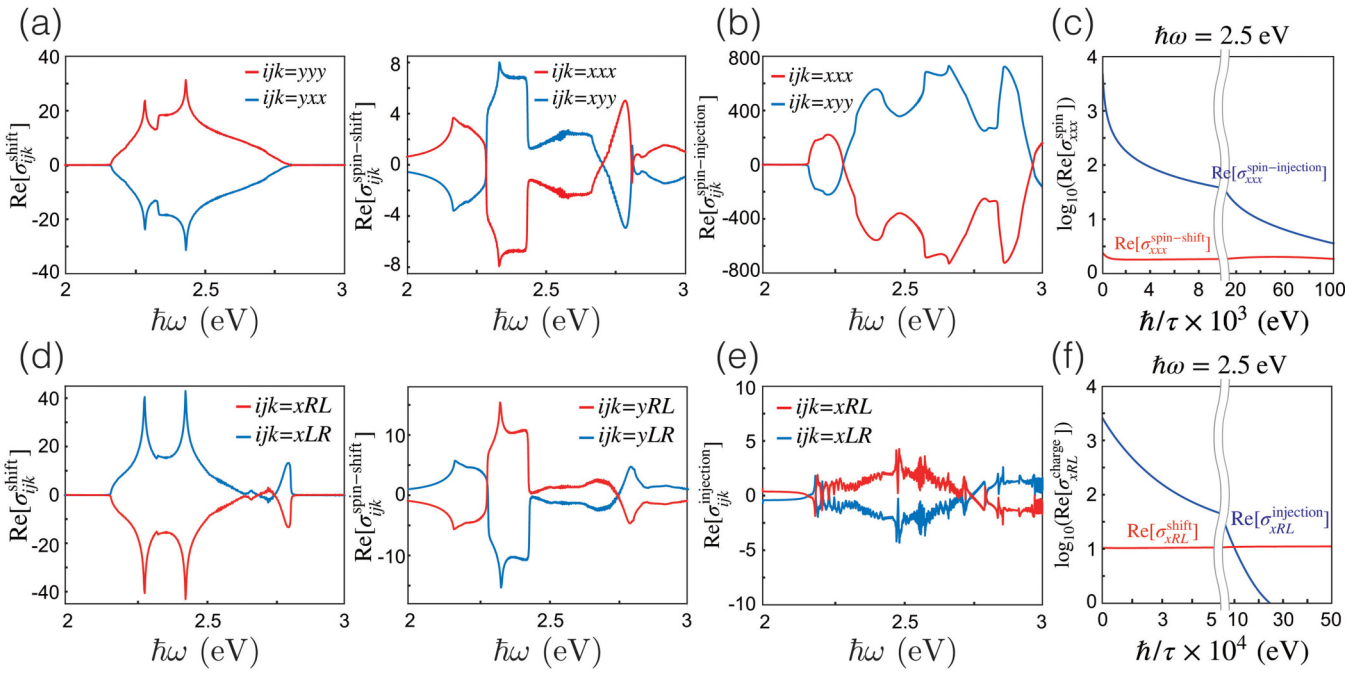

FIG. 5. Real parts of charge and spin (a), (d) shift- and injection-current (b), (e) conductivities for monolayer $NbSe_2$ under LP and CP light irradiation, respectively. (c), (f) τ dependencies of shift- (red) and injection- (blue) current conductivities for linearly x-polarized and RCP light of $\hbar\omega = 2.5$ eV. Here, plots of the NLO conductivities are shown in logarithmic scale. The units of NLO charge and spin conductivities are $e^3/\hbar$ and e^2, respectively.

B. Shift and injection currents under CP light irradiation

Similarly, for irradiation of CP light, the shift- and injection-current conductivities are given as

$$\sigma^{\text{shift}}_{iRL}(0;\omega,-\omega) = \frac{e^3}{\hbar S}\sum_{\boldsymbol{k}}\sum_{mn} f_{nm}\frac{\Omega^{xy}_{mn}(\boldsymbol{k}) - \Omega^{yx}_{mn}(\boldsymbol{k})}{E_{mn} - \hbar\omega - i\eta}R^{i}_{nm}(\boldsymbol{k}) \tag{29}$$

and

$$\sigma^{\text{injection}}_{iRL}(0;\omega,-\omega) = \frac{\tau e^3}{\hbar S}\sum_{\boldsymbol{k}}\sum_{mn} f_{nm}\frac{\Omega^{xy}_{mn}(\boldsymbol{k}) - \Omega^{yx}_{mn}(\boldsymbol{k})}{E_{mn} - \hbar\omega - i\eta}\Delta^{i}_{mn}(\boldsymbol{k}) \tag{30}$$

with Berry curvature

$$\Omega^{xy}_{mn}(\boldsymbol{k}) = -\Omega^{yx}_{mn}(\boldsymbol{k}) = -\hbar^2\frac{\text{Im}\left[v^{x}_{mn}(\boldsymbol{k})v^{y}_{nm}(\boldsymbol{k})\right]}{E^2_{mn}}. \tag{31}$$

Note that the subscript RL means irradiation of RCP light. If these conductivities include the spin current operator, Eqs. (29) and (30) are rewritten as spin-dependent shift- and injection-current conductivities. Here, $R^{i}_{nm}(\boldsymbol{k})$ and $\Delta^{i}_{mn}(\boldsymbol{k})$ include the charge and spin operators.

For RCP light, the finite elements of charge and spin shift-current conductivities are $\sigma^{\text{shift}}_{xRL}(0;\omega,-\omega)$ and $\sigma^{\text{spin shift}}_{yRL}(0;\omega,-\omega)$. For LCP light, the charge and spin shift-current conductivities have opposite sign to those of RCP light, i.e.,

$$\begin{aligned}\sigma^{\text{shift}}_{xLR}(0;\omega,-\omega) &= -\sigma^{\text{shift}}_{xRL}(0;\omega,-\omega),\\ \sigma^{\text{spin shift}}_{yLR}(0;\omega,-\omega) &= -\sigma^{\text{spin shift}}_{yRL}(0;\omega,-\omega).\end{aligned} \tag{32}$$

The other elements are absent for monolayer $NbSe_2$.

Figure 5(d) shows the charge and spin shift-current conductivities for monolayer $NbSe_2$ under irradiation of CP light. Because of the broken inversion symmetry, the charge shift current can be generated in the x direction for CP light. On the other hand, the spin shift current can be generated in the y-direction for CP light. Comparing the results of CP light with those of LP light, the directions of generated charge and spin shift current are switched for monolayer $NbSe_2$: the charge shift current is generated in the y direction for LP light, but in the x direction for CP light. For spin shift current, the irradiation of LP and CP light causes the generation in x and y directions, respectively. Thus, the direction of generated shift current can be switched if LP light is altered to CP light.

For CP light, the charge injection-current conductivities $\sigma^{\text{injection}}_{xRL}(0;\omega,-\omega)$ and $\sigma^{\text{injection}}_{xLR}(0;\omega,-\omega)$ are finite for monolayer $NbSe_2$; in addition, the relation of these finite conductivities is given as

$$\sigma^{\text{injection}}_{xRL}(0;\omega,-\omega) = -\sigma^{\text{injection}}_{xLR}(0;\omega,-\omega). \tag{33}$$

The other elements are absent for monolayer $NbSe_2$.

Figure 5(e) shows the charge injection-current conductivities for monolayer $NbSe_2$ under irradiation of CP light. Owing to the broken inversion symmetry, the charge injection current can be generated in the x direction for CP light. As shown in Fig. 5(f), the magnitude of injection-current conductivity becomes larger with the increase of τ, but that of shift-current conductivity is robust owing to its topological properties. It is found that the generated injection current for CP light irradiation has stronger τ dependence than that of LP light.

$\Omega^{xy}_{mn}(\boldsymbol{k})$, $R^{i}_{nm}(\boldsymbol{k})$, and $\Delta^{i}_{mn}(\boldsymbol{k})$ of the integrands in Eqs. (29) and (30) are shown in Appendix E. Since the products are even

TABLE II. Shift- and injection-current conductivities for monolayer $NbSe_2$ under irradiation of LP and CP light.

	$\sigma_{ijk}^{\text{shift}}(0;\omega,-\omega)$	$\sigma_{ijk}^{\text{spin shift}}(0;\omega,-\omega)$	$\sigma_{ijk}^{\text{injection}}(0;\omega,-\omega)$	$\sigma_{ijk}^{\text{spin injection}}(0;\omega,-\omega)$
$ijk = xxx$	0	$\approx 10^0$	0	$\approx 10^2$ ($\eta = 0.001$ eV)
$ijk = xyy, yxy, yyx$	0	$\approx -10^0$	0	$\approx -10^2$ ($\eta = 0.001$ eV)
$ijk = yyy$	$\approx 10^1$	0	0	0
$ijk = yxx, xyx, xxy$	$\approx -10^1$	0	0	0
$ijk = xRL$	$\approx 10^1$	0	$\approx 10^1$ ($\eta = 0.001$ eV)	0
$ijk = yRL$	0	$\approx 10^1$	0	0
$ijk = xLR$	$\approx -10^1$	0	$\approx -10^1$ ($\eta = 0.001$ eV)	0
$ijk = yLR$	0	$\approx -10^1$	0	0

for π rotation, where $\Omega_{mn}^{xy}(\boldsymbol{k})$, $R_{nm}^{i}(\boldsymbol{k})$, and $\Delta_{mn}^{i}(\boldsymbol{k})$ are odd, the shift and injection currents can be generated for monolayer $NbSe_2$. However, when the products are odd for π rotation, the current is absent.

C. Selection rule by polarization

The selection rules of shift- and injection-current conductivities by light polarization are summarized in Table II. Figures 6(a) and 6(b) show the schematics of generated shift current in monolayer $NbSe_2$ under irradiation of LP light. For y-polarized light, the charge and spin shift currents can be generated in y and x directions. On the other hand, for x-polarized light, the charge and spin shift currents are generated in y and x directions, respectively. For CP light irradiation, the charge and spin shift currents can be generated in x and y directions as shown in Figs. 6(c) and 6(d). Thus, the directions of generated charge and spin shift currents are switched when the polarization of incident light is altered from LP to CP.

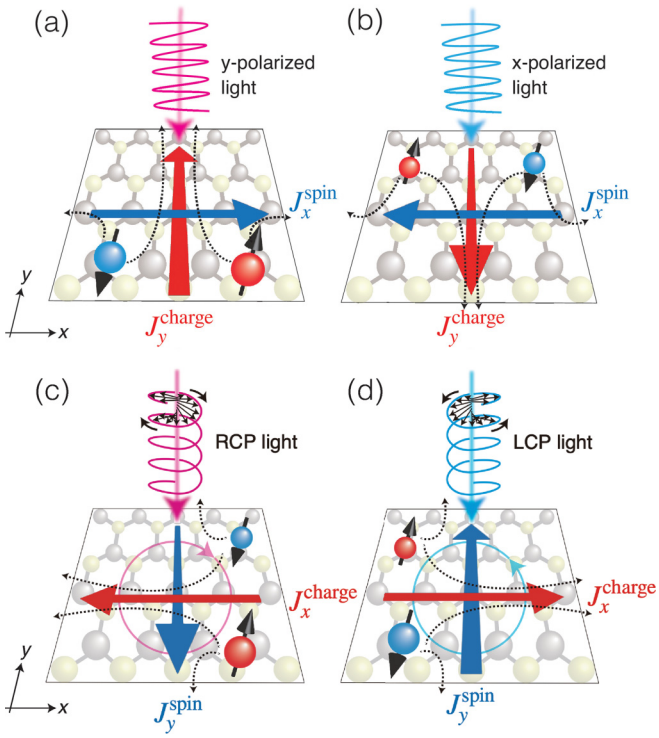

FIG. 6. Schematics of generated charge and spin shift currents for (a) y-polarized light and (b) x-polarized light in monolayer $NbSe_2$. For (c) RCP and (d) LCP light, generation of charge and spin shift currents is caused in monolayer $NbSe_2$.

VI. SUMMARY

In summary, we have theoretically studied the second-order NLO charge and spin currents in the metallic TMDCs. As an example of metallic TMDCs, we have employed few-layered $NbSe_2$, which possesses the Ising-type SOC. For odd-number-layered $NbSe_2$, the inversion symmetry is broken, however, the inversion symmetry is preserved for even-number-layered $NbSe_2$. It is pointed out that the second-order NLO charge and spin currents in the metallic TMDCs strongly depend on their crystal symmetry of system and polarization of incident light. The NLO current is finite for odd-number-layered $NbSe_2$, but absent for even-number-layered $NbSe_2$.

Since BCL can control the symmetry of electronic system, NLO charge and spin currents can be induced along the directions of leaves of BCL. Thus, under irradiation of BCL, the NLO current can be generated in not only odd-number-layered, but also even-number-layered $NbSe_2$. For even-number-layered $NbSe_2$, the peaks appear in low-energy range, which cause the infrared light absorption. Such infrared light absorption is absent in semiconductor TMDC owing to the energy band gap around the Fermi level.

In addition, we have shown that shift and injection current can be generated in odd-number-layered $NbSe_2$ under irradiation of LP and CP light. The topological shift current is robust to electron scattering of the system, but the injection current strongly depends on the scattering. The generated shift current can be switched if LP light is altered to CP light.

In the Supplemental Material, the second-order NLO current can be generated even in MoS_2 as a reference of TMDC semiconductors [63]. Thus, TMDCs such as $NbSe_2$ and MoS_2 can be used for the source of second-order NLO charge and spin currents. Our results can serve to design spin current harvesting and opto-spintronics devices on the basis of 2D materials.

ACKNOWLEDGMENTS

This work was supported by JSPS KAKENHI (Grants No. 22H05473, No. JP21H01019, No. JP18H01154) and JST CREST (Grant No. JPMJCR19T1).

APPENDIX A: CRYSTAL SYMMETRY AND THE SECOND-ORDER NLO CONDUCTIVITY

The second-order NLO conductivity strongly depends on the crystal symmetry [28,62]. Table I shows that the NLO charge and spin conductivities of the SHG process are finite for odd-number-layered $NbSe_2$, but absent for even-number-layered $NbSe_2$. The finite NLO conductivities are attributed to the broken inversion symmetry. In this section, we discuss general NLO conductivities by considering the crystal symmetry of the system, which are consistent with the numerical results.

Even-number-layered $NbSe_2$ has the inversion-symmetric operator $\hat{P} = \hat{M}_x\hat{M}_y\hat{M}_z$. Here, the 3×3 matrices of $\hat{M}_x$, $\hat{M}_y$, and $\hat{M}_z$ are expressed as

$$\hat{M}_x = \begin{pmatrix} -1 & 0 & 0 \\ 0 & 1 & 0 \\ 0 & 0 & 1 \end{pmatrix},$$

$$\hat{M}_y = \begin{pmatrix} 1 & 0 & 0 \\ 0 & -1 & 0 \\ 0 & 0 & 1 \end{pmatrix},$$

$$\hat{M}_z = \begin{pmatrix} 1 & 0 & 0 \\ 0 & 1 & 0 \\ 0 & 0 & -1 \end{pmatrix}.$$

Because of the inversion symmetry P, position operator $\hat{\boldsymbol{r}}$, momentum operator $\hat{\boldsymbol{p}}$, and spin operator $\hat{\boldsymbol{s}} = \frac{\hbar}{2}(\hat{\sigma}_x, \hat{\sigma}_y, \hat{\sigma}_z)$ have the following properties:

$$\hat{P}\hat{\boldsymbol{r}} = -\hat{\boldsymbol{r}},\ \hat{P}\hat{\boldsymbol{p}} = -\hat{\boldsymbol{p}},\ \hat{P}\hat{\boldsymbol{s}} = \hat{\boldsymbol{s}}. \tag{A1}$$

The charge current density J_i^{charge} and j and k elements of incident electric fields $E_j(\omega_1)$ and $E_k(\omega_2)$ after the operation of $\hat{P}$ become

$$J_i^{\text{charge}} \xrightarrow{\hat{P}} \tilde{J}_i^{\text{charge}} = -J_i^{\text{charge}},$$

$$E_j(\omega_1)E_k(\omega_2) \xrightarrow{\hat{P}} \tilde{E}_j(\omega_1)\tilde{E}_k(\omega_2) = (-1)^2 E_j(\omega_1)E_k(\omega_2),$$

where i is the propagation of charge current ($i = x, y, z$) and (j, k) are the polarizations of incident light. Note that $\tilde{A}$ means the arbitrary physical quantity A after the symmetry operation. For second-order NLO response, J_i^{charge} is proportional to $E_j(\omega_1)E_k(\omega_2)$, which is given as

$$J_i^{\text{charge}} = \sigma_{ijk}^{\text{charge}}(\omega_1 + \omega_2; \omega_1, \omega_2)E_j(\omega_1)E_k(\omega_2). \tag{A2}$$

Comparing the current and electric fields before and after $\hat{P}$ operation, the NLO conductivities become

$$\sigma_{ijk}^{\text{charge}}(\omega_1 + \omega_2; \omega_1, \omega_2) = -\sigma_{ijk}^{\text{charge}}(\omega_1 + \omega_2; \omega_1, \omega_2).$$

Thus, in even-number-layered $NbSe_2$, the NLO charge conductivity $\sigma_{ijk}^{\text{charge}}(\omega_1 + \omega_2; \omega_1, \omega_2)$ is absent for all combinations of ijk.

The spin current density J_i^{spin} is given as

$$J_i^{\text{spin}} = \sigma_{ijk}^{\text{spin}}(\omega_1 + \omega_2; \omega_1, \omega_2)E_j(\omega_1)E_k(\omega_2). \tag{A3}$$

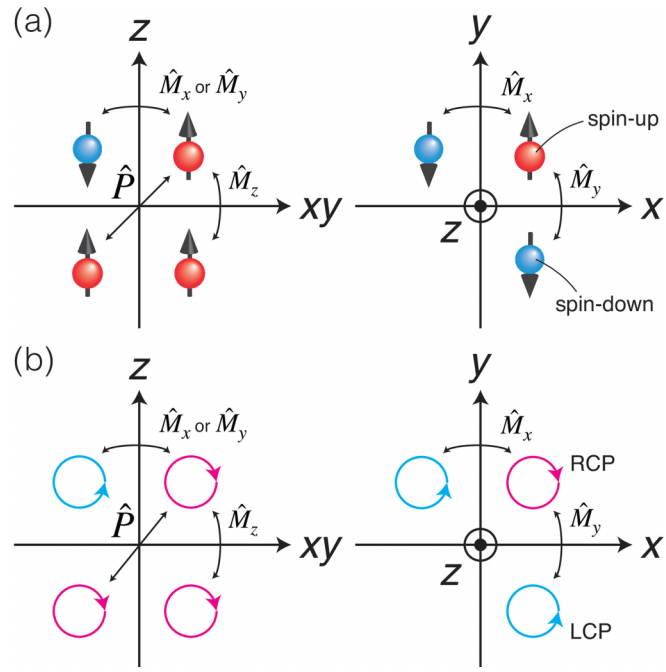

FIG. 7. Symmetric operator for an axial vector. Schematics of mirror and inversion symmetry operations $\hat{M}_x$, $\hat{M}_y$, $\hat{M}_z$, and $\hat{P}$ for (a) spin-up (red) and spin-down (blue) states $s_z = \pm\frac{\hbar}{2}$ and (b) electric fields of RCP (magenta) and LCP (cyan) light.

As seen in Fig. 7(a), in even-number-layered $NbSe_2$, the spin state is invariant after $\hat{P}$. Thus, J_i^{spin} after $\hat{P}$ becomes

$$J_i^{\text{spin}} \xrightarrow{\hat{P}} \tilde{J}_i^{\text{spin}} = -J_i^{\text{spin}},$$

which causes the absence of NLO spin conductivity $\sigma_{ijk}^{\text{spin}}(\omega_1 + \omega_2; \omega_1, \omega_2)$ for even-number-layered $NbSe_2$. These results are consistent with the numerical calculations shown in Table I.

In odd-number-layered $NbSe_2$, where P is broken, the system has the mirror symmetry M_xM_z. J_i^{charge} and $E_j(\omega_1)$, $E_k(\omega_2)$ after the mirror symmetry operation $\hat{M}_x\hat{M}_z$ become

$$J_i^{\text{charge}} \xrightarrow{\hat{M}_x\hat{M}_z} \tilde{J}_i^{\text{charge}} = (-1)^{\delta_{ix}+\delta_{iz}} J_i^{\text{charge}},$$

$$E_j(\omega_1) \xrightarrow{\hat{M}_x\hat{M}_z} \tilde{E}_j(\omega_1) = (-1)^{\delta_{jx}+\delta_{jz}} E_j(\omega_1),$$

$$E_k(\omega_2) \xrightarrow{\hat{M}_x\hat{M}_z} \tilde{E}_k(\omega_2) = (-1)^{\delta_{kx}+\delta_{kz}} E_k(\omega_2),$$

where δ_{ix} is the Kronecker delta:

$$\delta_{ix} = \begin{cases} 1 & (i = x), \\ 0 & (i \neq x). \end{cases} \tag{A4}$$

Thus, $\hat{M}_x\hat{M}_z$ makes the following ijk elements of $\sigma_{ijk}^{\text{charge}}(\omega_1 + \omega_2; \omega_1, \omega_2)$ in Eq. (A2) finite, i.e., $ijk = xxy, xyx, xyz, xzy, yxx, yxz, yyy, yzx, yzz, zxy, zyx, zyz, zzy$. The other elements are absent for odd-number-layered $NbSe_2$. In addition, the system has threefold rotation symmetry

operation $\hat{C}_3$, which is given as

$$\hat{C}_3 = \begin{pmatrix} -\frac{1}{2} & \frac{\sqrt{3}}{2} & 0 \\ -\frac{\sqrt{3}}{2} & -\frac{1}{2} & 0 \\ 0 & 0 & 1 \end{pmatrix}.$$

Owing to $\hat{C}_3$, the finite NLO charge conductivities have a relation for odd-number-layered $NbSe_2$, i.e.,

$$\begin{aligned}\sigma^{\text{charge}}_{yyy}(\omega_1+\omega_2;\omega_1,\omega_2) &= -\sigma^{\text{charge}}_{xxy}(\omega_1+\omega_2;\omega_1,\omega_2) \\ &= -\sigma^{\text{charge}}_{xyx}(\omega_1+\omega_2;\omega_1,\omega_2) \\ &= -\sigma^{\text{charge}}_{yxx}(\omega_1+\omega_2;\omega_1,\omega_2).\end{aligned} \tag{A5}$$

In Fig. 7(a), the spin state becomes opposite after $\hat{M}_x\hat{M}_z$, which causes

$$J^{\text{spin}}_i \xrightarrow{\hat{M}_x\hat{M}_z} \tilde{J}^{\text{spin}}_i = -(-1)^{\delta_{ix}+\delta_{iz}} J^{\text{spin}}_i.$$

Thus, the following ijk elements of $\sigma^{\text{spin}}_{ijk}(\omega_1+\omega_2;\omega_1,\omega_2)$ in Eq. (A3) are finite for odd-number-layered $NbSe_2$: $ijk = xxx, xxz, xyy, xzx, xzz, yxy, yyx, yyz, yzy, zxx, zxz, zyy, zzx, zzz$. The other elements are absent. Also, for odd-number-layered $NbSe_2$, the following relation of $\sigma^{\text{spin}}_{ijk}(\omega_1+\omega_2;\omega_1,\omega_2)$ is obtained after $\hat{C}_3$, i.e.,

$$\begin{aligned}\sigma^{\text{spin}}_{xxx}(\omega_1+\omega_2;\omega_1,\omega_2) &= -\sigma^{\text{spin}}_{xyy}(\omega_1+\omega_2;\omega_1,\omega_2) \\ &= -\sigma^{\text{spin}}_{yxy}(\omega_1+\omega_2;\omega_1,\omega_2) \\ &= -\sigma^{\text{spin}}_{yyx}(\omega_1+\omega_2;\omega_1,\omega_2).\end{aligned} \tag{A6}$$

These results indicate that spin current can be generated in odd-number-layered $NbSe_2$ when charge current is absent. When $\omega_1 = \omega_2 \equiv \omega \neq 0$, the analytic results are consistent with the numerical results of the SHG process shown in Table I.

Next, by considering the crystal symmetry, we shall discuss the generation of NLO charge and spin current in $NbSe_2$ under CP light irradiation. For CP light, J^{charge}_i is given as

$$J^{\text{charge}}_i = \sigma^{\text{charge}}_{iRL}(\omega_1+\omega_2;\omega_1,\omega_2)E_R(\omega_1)E_L(\omega_2). \tag{A7}$$

For even-number-layered $NbSe_2$, the product of electric fields of CP light $E_R(\omega_1)E_L(\omega_2)$ after $\hat{P}$ becomes

$$E_R(\omega_1)E_L(\omega_2) \xrightarrow{\hat{P}} \tilde{E}_R(\omega_1)\tilde{E}_L(\omega_2) = E_R(\omega_1)E_L(\omega_2),$$

where as shown in Fig. 7(b), $E_R(\omega_1)$, $E_L(\omega_2)$ are invariant for $\hat{P}$. Comparing the current and the electric fields of incident light before and after $\hat{P}$, $\sigma^{\text{charge}}_{iRL}(\omega_1+\omega_2;\omega_1,\omega_2)$ becomes zero. Since J^{spin}_i is invariant after $\hat{P}$, $\sigma^{\text{spin}}_{iRL}(\omega_1+\omega_2;\omega_1,\omega_2)$ is absent as same as NLO charge conductivity.

In odd-number-layered $NbSe_2$, $E_R(\omega_1)E_L(\omega_2)$ after $\hat{M}_x\hat{M}_z$ becomes

$$E_R(\omega_1)E_L(\omega_2) \xrightarrow{\hat{M}_x\hat{M}_z} \tilde{E}_R(\omega_1)\tilde{E}_L(\omega_2) = E_L(\omega_1)E_R(\omega_2).$$

Thus, $\hat{M}_x\hat{M}_z$ makes $\sigma^{\text{charge}}_{xRL}(\omega_1+\omega_2;\omega_1,\omega_2)$ and $\sigma^{\text{charge}}_{zRL}(\omega_1+\omega_2;\omega_1,\omega_2)$ finite, but $\sigma^{\text{charge}}_{yRL}(\omega_1+\omega_2;\omega_1,\omega_2)$ is absent. Since the spin state becomes opposite owing to $\hat{M}_x\hat{M}_z$, the NLO spin conductivity $\sigma^{\text{spin}}_{yRL}(\omega_1+\omega_2;\omega_1,\omega_2)$ is finite, but the other elements are absent. These results are consistent with the numerical calculation summarized in Table II.

In addition, under irradiation of BCL [$A_{\text{BCL}}(t) = A_L e^{in_1\omega t} + A_R e^{in_2\omega t - i\theta}$ + c.c.], the mirror symmetry M_x is broken. Thus, $\hat{M}_y\hat{M}_z$ remains in the electronic system. J^{charge}_i and $E_{\text{BCL}}(t)$ after $\hat{M}_y\hat{M}_z$ become

$$J^{\text{charge}}_i \xrightarrow{\hat{M}_y\hat{M}_z} \tilde{J}^{\text{charge}}_i = (-1)^{\delta_{iy}+\delta_{iz}} J^{\text{charge}}_i,$$

$$E_{\text{BCL}}(t) \xrightarrow{\hat{M}_y\hat{M}_z} \tilde{E}_{\text{BCL}}(t) = E_{\text{BCL}}(t).$$

Comparing the current and the electric field of incident light before and after $\hat{M}_y\hat{M}_z$, the NLO charge conductivity $\sigma^{\text{charge}}_{x\text{-BCL-BCL}}(n_1\omega, n_2\omega)$ becomes finite. However, the other elements are absent for even-number-layered $NbSe_2$. As seen in Fig. 7(a), for $\hat{M}_y\hat{M}_z$, the spin state becomes opposite. Thus, $\sigma^{\text{spin}}_{y\text{-BCL-BCL}}(n_1\omega, n_2\omega)$ and $\sigma^{\text{spin}}_{z\text{-BCL-BCL}}(n_1\omega, n_2\omega)$ are finite, but $\sigma^{\text{spin}}_{x\text{-BCL-BCL}}(n_1\omega, n_2\omega)$ is absent. These analytic results show that thanks to incident BCL, the NLO charge and spin currents can be generated even in even-number-layered $NbSe_2$.

Odd-number-layered $NbSe_2$ has M_xM_z. Since M_x is broken under BCL irradiation, the electronic system has $\hat{M}_z$. For $\hat{M}_z$, J^{charge}_i and $E_{\text{BCL}}(t)$ become

$$J^{\text{charge}}_i \xrightarrow{\hat{M}_z} \tilde{J}^{\text{charge}}_i = (-1)^{\delta_{iz}} J^{\text{charge}}_i,$$

$$E_{\text{BCL}}(t) \xrightarrow{\hat{M}_z} \tilde{E}_{\text{BCL}}(t) = E_{\text{BCL}}(t).$$

Owing to the comparison between the generated current and incident light before and after $\hat{M}_z$, $\sigma^{\text{charge}}_{x\text{-BCL-BCL}}(n_1\omega, n_2\omega)$ and $\sigma^{\text{charge}}_{y\text{-BCL-BCL}}(n_1\omega, n_2\omega)$ become finite for odd-number-layered $NbSe_2$, but $\sigma^{\text{charge}}_{z\text{-BCL-BCL}}(n_1\omega, n_2\omega)$ is absent. Since the spin state is invariant after $\hat{M}_z$, $\sigma^{\text{spin}}_{x\text{-BCL-BCL}}(n_1\omega, n_2\omega)$ and $\sigma^{\text{spin}}_{y\text{-BCL-BCL}}(n_1\omega, n_2\omega)$ are finite, but $\sigma^{\text{spin}}_{z\text{-BCL-BCL}}(n_1\omega, n_2\omega)$ is absent.

APPENDIX B: NLO CHARGE AND SPIN CONDUCTIVITIES FOR IRRADIATION OF BCL WITH MULTILEAVES

In this Appendix, we consider BCL of four, five, six, and seven leaves with $\theta = 0$ in Eq. (12). Figure 8(a) shows the trajectories of these incident BCL. Figures 8(b)–8(e) show the NLO charge and spin conductivities for monolayer $NbSe_2$ with SOC under irradiation of BCL. Since the BCL can control the symmetry of electronic system, these NLO charge and spin conductivities are finite for monolayer $NbSe_2$, which are similar to the results of BCL with three leaves ($n_1 : n_2 = 1 : 2$). Thus, unlike the irradiation of LP light, the NLO charge and spin currents are generated in both x and y directions along the induced polarizations by irradiating BCL.

We should note that the peaks of the NLO charge and spin conductivities shift lower with increase of leaves of BCL. The shift originates from the denominator $E_{mn} - (n_1+n_2)\hbar\omega - i\eta$ in Eq. (9). With increase of (n_1+n_2), the denominator $E_{mn} - (n_1+n_2)\hbar\omega - i\eta$ becomes smaller, thus the shift occurs.

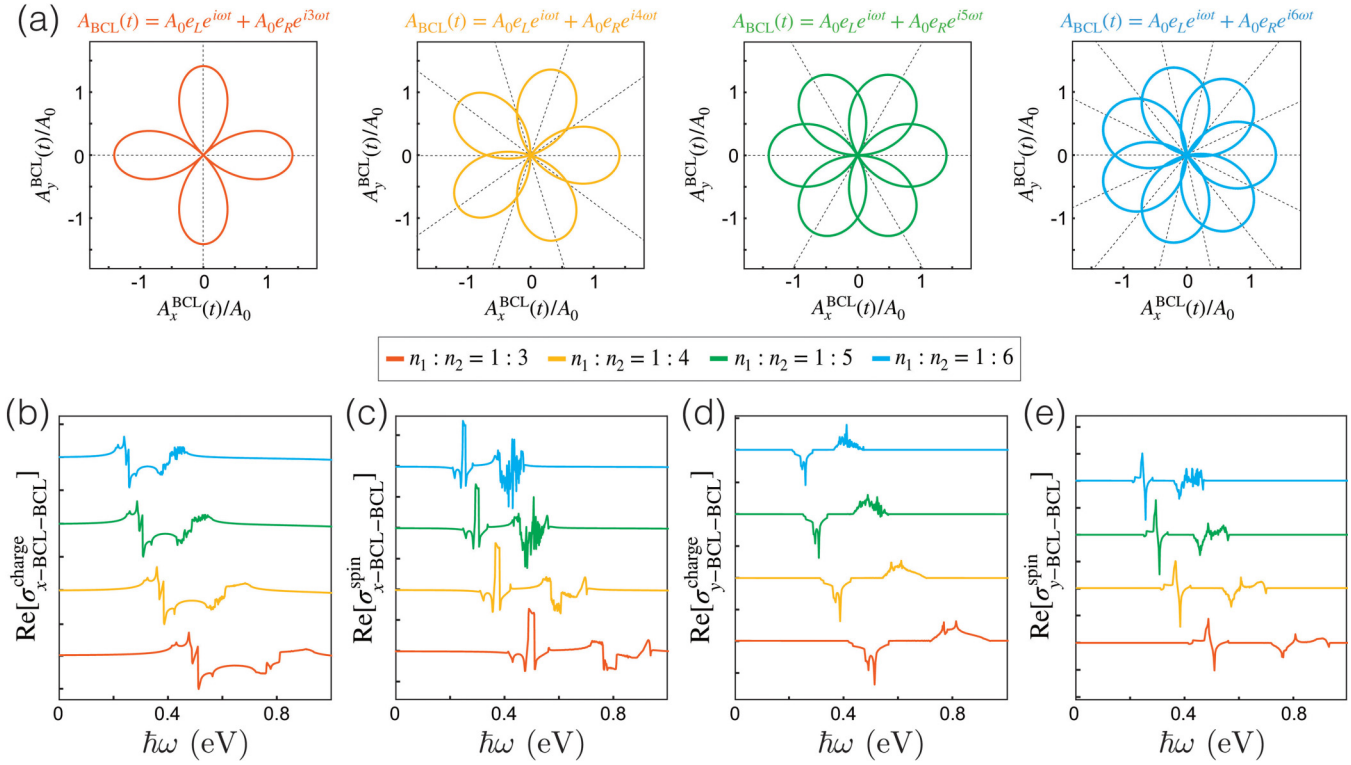

FIG. 8. (a) Trajectories of BCL with four, five, six, and seven leaves. Real parts of NLO charge and spin conductivities (b) $\sigma^{charge}_{x\text{-BCL-BCL}}$, (c) $\sigma^{spin}_{x\text{-BCL-BCL}}$, (d) $\sigma^{charge}_{y\text{-BCL-BCL}}$, and (e) $\sigma^{spin}_{y\text{-BCL-BCL}}$ for monolayer $NbSe_2$ with SOC under irradiation of BCL. Orange, yellow, green, and blue lines indicate NLO conductivities for BCL with four, five, six, and seven leaves. The units of NLO charge and spin conductivities are $e^3/\hbar$ and e^2, respectively.

APPENDIX C: FINITE CONDUCTIVITY FOR CP LIGHT WITH DIFFERENT OPTICAL ANGULAR FREQUENCY

The shift current under irradiation of CP light contains the product of Berry curvature $\Omega^{xy}_{mn}(\boldsymbol{k})$ and shift vector $R^i_{nm}(\boldsymbol{k})$ as shown in Eq. (29). The Berry curvatures between RCP and LCP light are antisymmetric, thus, the shift current for irradiation of RCP and LCP light is generated in opposite directions.

When the optical angular frequencies of RCP and LCP light are the same, as shown in Fig. 9(a), the cancellation of generated shift current occurs for RCP and LCP light, i.e., absence of current [42,80,81]. Figure 9(b) shows the schematics of shift current under the irradiation of LCP light with $2n_1\omega$ and RCP light with $2n_2\omega$. If LCP and RCP light have different optical angular frequencies, i.e., $n_1 \neq n_2$, the amounts of shifts for photoexcited electrons under irradiation of LCP and RCP light are not the same, i.e., no cancellation of shift current.

In Eq. (13), the NLO conductivity for BCL irradiation is rewritten as the summation of conductivities for four different combinations of CP light, i.e., *LL*, *LR*, *RL*, *RR*. Owing to the irradiation of CP light with different optical angular frequencies, the first and fourth terms are finite, but other terms are canceled. Thus, for irradiation of BCL, the second-order NLO current is generated even in even-number-layered $NbSe_2$.

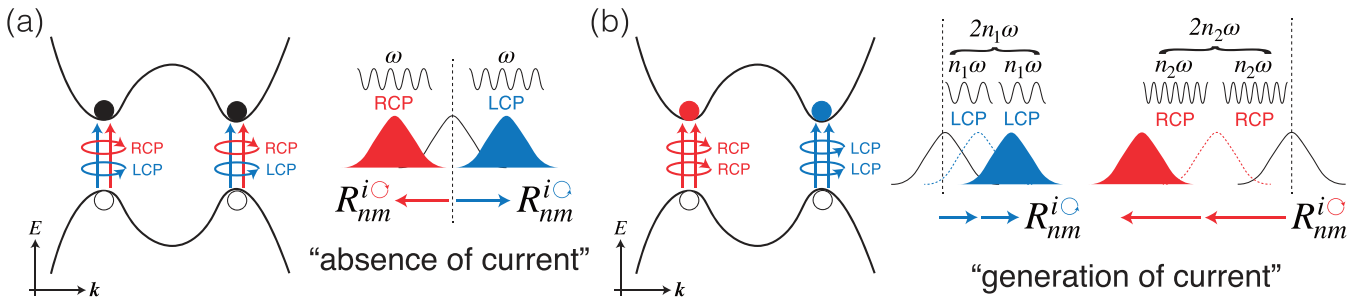

FIG. 9. Schematics of photoexcitation for CP light irradiation and corresponding shift vectors. (a) For irradiation of RCP (red) and LCP (blue) light with same optical angular frequency ω, RCP and LCP make the same amount of shift but opposite direction, i.e., absence of current. (b) For irradiation of RCP and LCP light with different optical angular frequencies $n_1\omega \neq n_2\omega$, the amount of shifts by RCP and LCP is different and no cancellation, i.e., generation of current.

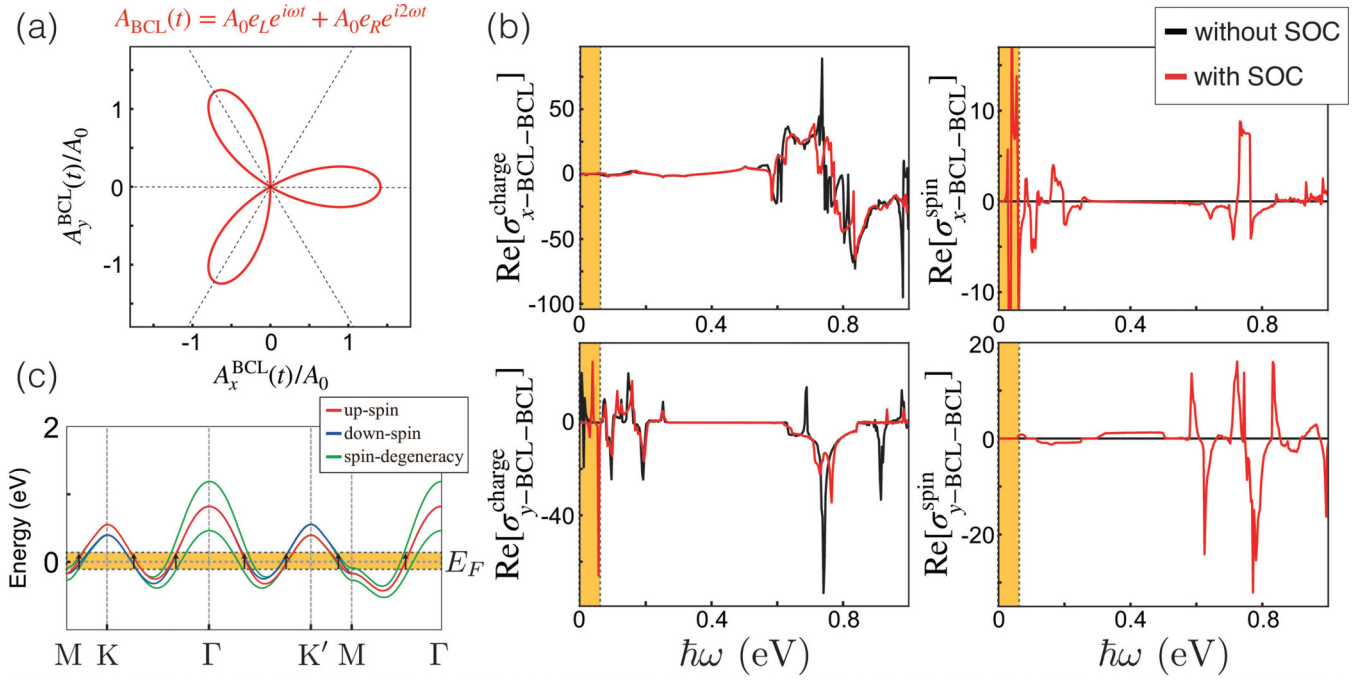

FIG. 10. (a) Trajectory of BCL with three leaves ($n_1 : n_2 = 1 : 2$). (b) Real parts of NLO charge and spin conductivities $\sigma^{\rm charge}_{x\text{-BCL-BCL}}$, $\sigma^{\rm spin}_{x\text{-BCL-BCL}}$, $\sigma^{\rm charge}_{y\text{-BCL-BCL}}$, and $\sigma^{\rm spin}_{y\text{-BCL-BCL}}$ for trilayer $NbSe_2$. Black and red lines indicate NLO conductivities without and with SOC. The units of NLO charge and spin conductivities are $e^3/\hbar$ and e^2, respectively. (c) Energy band structure of trilayer $NbSe_2$ and the interband optical transition between nearest valence and conduction bands around Fermi energy $E_F = 0$ eV (shown by a yellow square).

APPENDIX D: NLO CHARGE AND SPIN CURRENTS IN TRILAYER $NbSe_2$ UNDER IRRADIATION OF BCL

As shown in Fig. 10(a), we consider $n_1 : n_2 = 1 : 2$ and $\theta = 0$ for BCL with three leaves. Figure 10(b) shows the NLO charge and spin conductivities for trilayer $NbSe_2$ under irradiation of the BCL. Since the BCL breaks the mirror symmetry with respect to the y-z plane, these NLO charge and spin conductivities are finite for trilayer $NbSe_2$. Here, it should be noted that the peaks of the NLO conductivities appear around $\hbar\omega = 0.01$ eV shown by yellow squares. The appearance of peaks occurs owing to the photoexcitation between the nearest valence and conduction bands of trilayer $NbSe_2$ as shown in Fig. 10(c), which causes infrared light absorption.

In addition, for trilayer $NbSe_2$, the NLO conductivities under irradiation of three-leaf BCL consist of three optical transition processes: (i) intralayer optical transition of monolayer $NbSe_2$, (ii) intralayer and interlayer optical transitions of bilayer $NbSe_2$, and (iii) interlayer optical transition between monolayer and bilayer $NbSe_2$. For irradiation of LP light, the process (ii) is absent [62], however, BCL with three leaves makes all three processes finite.

APPENDIX E: CONTOUR PLOTS OF $\alpha^{jk}_{mn}(\boldsymbol{k})$, $R^i_{nm}(\boldsymbol{k})$, $\Delta^i_{mn}(\boldsymbol{k})$, $\Omega^{jk}_{mn}(\boldsymbol{k})$

We discuss the origin of finite shift and injection current by considering the contour plots of transition intensity $\alpha^{jk}_{mn}(\boldsymbol{k})$, shift vector $R^i_{nm}(\boldsymbol{k})$, velocity difference between electron and hole $\Delta^i_{mn}(\boldsymbol{k})$, and Berry curvature $\Omega^{jk}_{mn}(\boldsymbol{k})$. All these factors appear as the integrand of the conductivities. For simplicity, we shall focus on the results of monolayer $NbSe_2$ because other cases such bilayer and trilayer $NbSe_2$ are similar.

In Eq. (23), the charge (spin) shift-current conductivity for LP light contains the product $\alpha^{jk}_{mn}(\boldsymbol{k})$ $R^i_{nm}(\boldsymbol{k})$ $[\alpha^{jk}_{mn}(\boldsymbol{k})R^{i-\rm spin}_{nm}(\boldsymbol{k})]$. If the product $\alpha^{jk}_{mn}(\boldsymbol{k})R^i_{nm}(\boldsymbol{k})$ is even with respect to π rotation, the shift-current conductivities become finite. According to the contour plots of transition intensity shown in Fig. 11(a), $\alpha^{jk}_{mn}(\boldsymbol{k})$ with $jk = xx, yy$ is even for π rotation. Similarly, as shown in Fig. 11(b), the shift vectors $R^y_{nm}(\boldsymbol{k})$ and $R^{x-\rm spin}_{nm}(\boldsymbol{k})$ are also even for π rotation. Therefore, the charge and spin shift current are generated in y and x directions, respectively. The remaining elements $R^x_{nm}(\boldsymbol{k})$ and $R^{y\ \rm spin}_{nm}(\boldsymbol{k})$ are odd for π rotation, i.e., the absence of shift current.

In Eq. (25), the charge (spin) injection-current conductivity for LP light contains $\alpha^{jk}_{mn}(\boldsymbol{k})\Delta^i_{mn}(\boldsymbol{k})$ $[\alpha^{jk}_{mn}(\boldsymbol{k})\Delta^{i-\rm spin}_{mn}(\boldsymbol{k})]$. Since $\alpha^{jk}_{mn}(\boldsymbol{k})$ with $jk = xx, yy$ is even with respect to π rotation, velocity difference $\Delta^i_{mn}(\boldsymbol{k})$ should be even in order to generate the injection current. In actuality, as shown in Fig. 11(c), $\Delta^{x\ \rm spin}_{mn}(\boldsymbol{k})$ has even parity. Thus, the spin injection current is generated in the x direction. The remaining elements of $\Delta^i_{mn}(\boldsymbol{k})$ are odd, i.e., the absence of injection current.

Similarly, in Eqs. (29) and (30), the charge (spin) shift- and injection-current conductivities for RCP light contain the products $\Omega^{xy}_{mn}(\boldsymbol{k})R^i_{nm}(\boldsymbol{k})$ $[\Omega^{xy}_{mn}(\boldsymbol{k})R^{i-\rm spin}_{nm}(\boldsymbol{k})]$ and $\Omega^{xy}_{mn}(\boldsymbol{k})\Delta^i_{mn}(\boldsymbol{k})$ $[\Omega^{xy}_{mn}(\boldsymbol{k})\Delta^{i-\rm spin}_{mn}(\boldsymbol{k})]$, respectively. When the products are even with respect to π rotation, the shift and injection currents are generated for RCP light. Figures 11(d)–11(f) show the contour plots of Berry curvature, shift vector,

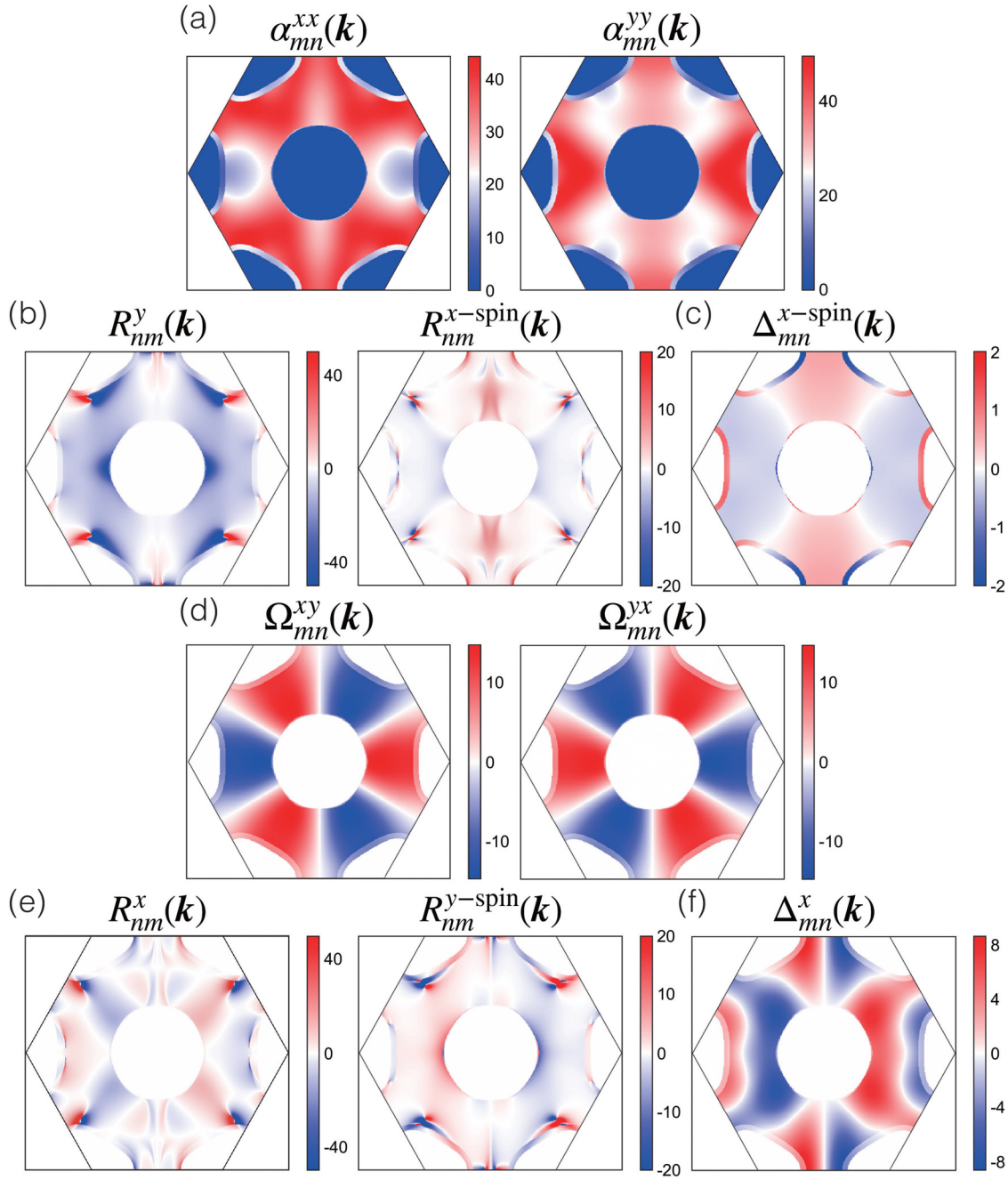

FIG. 11. Contour plots of shift- and injection-current conductivity components: (a) transition intensities $\alpha^{xx}_{mn}(\boldsymbol{k})$ and $\alpha^{yy}_{mn}(\boldsymbol{k})$, (b), (e) shift vectors $R^{y}_{nm}(\boldsymbol{k})$, $R^{x\,\mathrm{spin}}_{nm}(\boldsymbol{k})$, $R^{x}_{nm}(\boldsymbol{k})$, and $R^{y\,\mathrm{spin}}_{nm}(\boldsymbol{k})$, (c), (f) velocity difference between electron and hole $\Delta^{x\,\mathrm{spin}}_{mn}(\boldsymbol{k})$ and $\Delta^{x}_{mn}(\boldsymbol{k})$, and (d) Berry curvatures $\Omega^{xy}_{mn}(\boldsymbol{k})$ and $\Omega^{yx}_{mn}(\boldsymbol{k})$, respectively.

and velocity difference for monolayer $NbSe_2$ under RCP light irradiation. From Fig. 11(d), $\Omega^{xy}_{mn}(\boldsymbol{k})$ and $\Omega^{yx}_{mn}(\boldsymbol{k})$ are odd for π rotation. Since $R^{x}_{nm}(\boldsymbol{k})$ and $R^{y-\mathrm{spin}}_{nm}(\boldsymbol{k})$ are odd parities, the charge and spin shift currents are generated in x and y directions, respectively. Similarly, since $\Delta^{x}_{mn}(\boldsymbol{k})$ is odd parity, the charge injection current is generated in the x direction.

[1] P. A. Franken, A. E. Hill, C. W. Peters, and G. Weinreich, Generation of Optical Harmonics, Phys. Rev. Lett. **7**, 118 (1961).
[2] N. Bloembergen, *Nonlinear Optics*, 4th ed. (World Scientific, Singapore, 1996).
[3] R. W. Boyd, *Nonlinear Optics*, 3rd ed. (Academic Press, San Diego, 2008).
[4] J. E. Sipe and A. I. Shkrebtii, Second-order optical response in semiconductors, Phys. Rev. B **61**, 5337 (2000).

[5] X. Wen, Z. Gong, and D. Li, Nonlinear optics of two-dimensional transition metal dichalcogenides, InfoMat **1**, 317 (2019).

[6] M. L. Trolle, G. Seifert, and T. G. Pedersen, Theory of excitonic second-harmonic generation in monolayer MoS_2, Phys. Rev. B **89**, 235410 (2014).

[7] N. Kumar, S. Najmaei, Q. Cui, F. Ceballos, P. M. Ajayan, J. Lou, and H. Zhao, Second harmonic microscopy of monolayer mos_2, Phys. Rev. B **87**, 161403(R) (2013).

[8] D. J. Moss, J. E. Sipe, and H. M. van Driel, Empirical tight-binding calculation of dispersion in the second-order nonlinear optical constant for zinc-blende crystals, Phys. Rev. B **36**, 9708 (1987).

[9] E. Ghahramani, D. J. Moss, and J. E. Sipe, Full-band-structure calculation of second-harmonic generation in odd-period strained $(Si)_n/(Ge)_n$ superlattices, Phys. Rev. B **43**, 8990 (1991).

[10] L. M. Malard, T. V. Alencar, A. P. M. Barboza, K. F. Mak, and A. M. de Paula, Observation of intense second harmonic generation from MoS_2 atomic crystals, Phys. Rev. B **87**, 201401(R) (2013).

[11] K. L. Seyler, J. R. Schaibley, P. Gong, P. Rivera, A. M. Jones, S. Wu, J. Yan, D. G. Mandrus, W. Yao, and X. Xu, Electrical control of second-harmonic generation in a WSe_2 monolayer transistor, Nat. Nanotechnol. **10**, 407 (2015).

[12] S. N. Rashkeev, W. R. L. Lambrecht, and B. Segall, Efficient *abinitio* method for the calculation of frequency-dependent second-order optical response in semiconductors, Phys. Rev. B **57**, 3905 (1998).

[13] S. N. Rashkeev and W. R. L. Lambrecht, Second-harmonic generation of I-III-VI_2 chalcopyrite semiconductors: Effects of chemical substitutions, Phys. Rev. B **63**, 165212 (2001).

[14] S. Sharma and C. Ambrosch-Draxl, Second-Harmonic Optical Response from First Principles, Phys. Scr. **T109**, 128 (2004).

[15] R. Leitsmann, W. G. Schmidt, P. H. Hahn, and F. Bechstedt, Second-harmonic polarizability including electron-hole attraction from band-structure theory, Phys. Rev. B **71**, 195209 (2005).

[16] Y. R. Shen, Surface properties probed by second-harmonic and sum-frequency generation, Nature (London) **337**, 519 (1989).

[17] Y. R. Shen, Revisiting the basic theory of sum-frequency generation, J. Chem. Phys. **153**, 180901 (2020).

[18] T. Ishiyama, T. Imamura, and A. Morita, Theoretical Studies of Structures and Vibrational Sum Frequency Generation Spectra at Aqueous Interfaces, Chem. Rev. **114**, 8447 (2014).

[19] C. Stock, K. Zlatanov, and T. Halfmann, Third harmonic generation and microscopy, enhanced by a bias harmonic field, Opt. Commun. **457**, 124660 (2020).

[20] C. Winterfeldt, C. Spielmann, and G. Gerber, Colloquium: Optimal control of high-harmonic generation, Rev. Mod. Phys. **80**, 117 (2008).

[21] G. Vampa, C. R. McDonald, G. Orlando, D. D. Klug, P. B. Corkum, and T. Brabec, Theoretical Analysis of High-Harmonic Generation in Solids, Phys. Rev. Lett. **113**, 073901 (2014).

[22] T. Morimoto and N. Nagaosa, Topological nature of nonlinear optical effects in solids, Sci. Adv. **2**, e1501524 (2016).

[23] M. Nakamura, S. Horiuchi, F. Kagawa, N. Ogawa, T. Kurumaji, Y. Tokura, and M. Kawasaki, Shift current photovoltaic effect in a ferroelectric charge-transfer complex, Nat. Commun. **8**, 281 (2017).

[24] A. M. Cook, B. M. Fregoso, F. de Juan, S. Coh, and J. E. Moore, Design principles for shift current photovoltaics, Nat. Commun. **8**, 14176 (2017).

[25] B. M. Fregoso, T. Morimoto, and J. E. Moore, Quantitative relationship between polarization differences and the zone-averaged shift photocurrent, Phys. Rev. B **96**, 075421 (2017).

[26] Y. J. Zhang, T. Ideue, M. Onga, F. Qin, R. Suzuki, A. Zak, R. Tenne, J. H. Smet, and Y. Iwasa, Enhanced intrinsic photovoltaic effect in tungsten disulfide nanotubes, Nature (London) **570**, 349 (2019).

[27] Y. Zhang, T. Holder, H. Ishizuka, F. de Juan, N. Nagaosa, C. Felser, and B. Yan, Switchable magnetic bulk photovoltaic effect in the two-dimensional magnet CrI_3, Nat. Commun. **10**, 3783 (2019).

[28] H. Xu, H. Wang, J. Zhou, and J. Li, Pure spin photocurrent in non-centrosymmetric crystals: bulk spin photovoltaic effect, Nat. Commun. **12**, 4330 (2021).

[29] T. Akamatsu, T. Ideue, L. Zhou, Y. Dong, S. Kitamura, M. Yoshii, D. Yang, M. Onga, Y. Nakagawa, K. Watanabe, T. Taniguchi, J. Laurienzo, J. Huang, Z. Ye, T. Morimoto, H. Yuan, and Y. Iwasa, A van der Waals interface that creates in-plane polarization and a spontaneous photovoltaic effect, Science **372**, 68 (2021).

[30] A. M. Schankler, L. Gao, and A. M. Rappe, Large Bulk Piezophotovoltaic Effect of Monolayer 2H-MoS_2, J. Phys. Chem. Lett. **12**, 1244 (2021).

[31] T. Ideue and Y. Iwasa, Symmetry Breaking and Nonlinear Electric Transport in van der Waals Nanostructures, Annu. Rev. Condens. Matter Phys. **12**, 201 (2021).

[32] K. S. Novoselov, D. Jiang, F. Schedin, T. J. Booth, V. V. Khotkevich, S. V. Morozov, and A. K. Geim, Two-dimensional atomic crystals, Proc. Natl. Acad. Sci. USA **102**, 10451 (2005).

[33] S. B. Desai, S. R. Madhvapathy, M. Amani, D. Kiriya, M. Hettick, M. Tosun, Y. Zhou, M. Dubey, J. W. Ager, III, D. Chrzan, and A. Javey, Gold-Mediated Exfoliation of Ultralarge Optoelectronically-Perfect Monolayers, Adv. Mater. **28**, 4053 (2016).

[34] Z. Lin, A. McCreary, N. Briggs, S. Subramanian, K. Zhang, Y. Sun, X. Li, N. J. Borys, H. Yuan, S. K. Fullerton-Shirey, A. Chernikov, H. Zhao, S. McDonnell, A. M. Lindenberg, K. Xiao, B. J. LeRoy, M. Drndic, J. C. M. Hwang, J. Park, M. Chhowalla *et al.*, 2D materials advances: from large scale synthesis and controlled heterostructures to improved characterization techniques, defects and applications, 2D Mater. **3**, 042001 (2016).

[35] J. Yu, X. Hu, H. Li, X. Zhou, and T. Zhai, Large-scale synthesis of 2D metal dichalcogenides, J. Mater. Chem. C **6**, 4627 (2018).

[36] S. Wang, J.-K. Huang, M. Li, A. Azam, X. Zu, L. Qiao, J. Yang, and S. Li, Growth of High-Quality Monolayer Transition Metal Dichalcogenide Nanocrystals by Chemical Vapor Deposition and Their Photoluminescence and Electrocatalytic Properties, ACS Appl. Mater. Interfaces **13**, 47962 (2021).

[37] T. K. Fryett, A. Zhan, and A. Majumdar, Phase-matched nonlinear optics via patterning layered materials, Opt. Lett. **42**, 3586 (2017).

[38] J. He, D. Wei, and X. Wang, Quasi-phase matching for a nonlinear photonic waveguide enabled by monolayer transition-metal dichalcogenide arrays, J. Korean Phys. Soc. **79**, 380 (2021).

[39] R. Fei, X. Lu, and L. Yang, Intrinsic spin photogalvanic effect in nonmagnetic insulator, arXiv:2006.10690.

[40] M. Bieler, K. Pierz, and U. Siegner, Simultaneous generation of shift and injection currents in (110)-grown GaAs/AlGaAs quantum wells, J. Appl. Phys. **100**, 083710 (2006).

[41] B. M. Fregoso, Bulk photovoltaic effects in the presence of a static electric field, Phys. Rev. B **100**, 064301 (2019).

[42] Y. Ikeda, S. Kitamura, and T. Morimoto, Floquet engineering of electric polarization with two-frequency drive, Prog. Theor. Exp. Phys. **2022**, 04A101 (2022).

[43] K. M. Dorney, T. Fan, Q. L. D. Nguyen, J. L. Ellis, D. D. Hickstein, N. Brooks, D. Zusin, C. Gentry, C. Hernández-García, H. C. Kapteyn, and M. M. Murnane, Bright, single helicity, high harmonics driven by mid-infrared bicircular laser fields, Opt. Express **29**, 38119 (2021).

[44] T. V. Trevisan, P. V. Arribi, O. Heinonen, R.-J. Slager, and P. P. Orth, Bicircular Light Floquet Engineering of Magnetic Symmetry and Topology and Its Application to the Dirac Semimetal Cd_3As_2, Phys. Rev. Lett. **128**, 066602 (2022).

[45] A. Jiménez-Galán, R. E. F. Silva, O. Smirnova, and M. Ivanov, Lightwave control of topological properties in 2D materials for sub-cycle and non-resonant valley manipulation, Nat. Photonics **14**, 728 (2020).

[46] S. Odžak and D. B. Milošević, Bicircular-laser-field-assisted electron-ion radiative recombination, Phys. Rev. A **92**, 053416 (2015).

[47] E. Pisanty, S. Sukiasyan, and M. Ivanov, Spin conservation in high-order-harmonic generation using bicircular fields, Phys. Rev. A **90**, 043829 (2014).

[48] X. Xi, L. Zhao, Z. Wang, H. Berger, L. Forró, J. Shan, and K. F. Mak, Strongly enhanced charge-density-wave order in monolayer $NbSe_2$, Nat. Nanotechnol. **10**, 765 (2015).

[49] U. Chatterjee, J. Zhao, M. Iavarone, R. Di Capua, J. P. Castellan, G. Karapetrov, C. D. Malliakas, M. G. Kanatzidis, H. Claus, J. P. C. Ruff, F. Weber, J. van Wezel, J. C. Campuzano, R. Osborn, M. Randeria, N. Trivedi, M. R. Norman, and S. Rosenkranz, Emergence of coherence in the charge-density wave state of 2H-$NbSe_2$, Nat. Commun. **6**, 6313 (2015).

[50] J. A. Wilson, F. J. Di Salvo, and S. Mahajan, Charge-density waves and superlattices in the metallic layered transition metal dichalcogenides, Adv. Phys. **50**, 1171 (2001).

[51] S. Kim and Y.-W. Son, Quasiparticle energy bands and Fermi surfaces of monolayer $NbSe_2$, Phys. Rev. B **96**, 155439 (2017).

[52] W.-Y. He, B. T. Zhou, J. J. He, N. F. Q. Yuan, T. Zhang, and K. T. Law, Magnetic field driven nodal topological superconductivity in monolayer transition metal dichalcogenides, Commun. Phys. **1**, 40 (2018).

[53] X. Xi, Z. Wang, W. Zhao, J.-H. Park, K. T. Law, H. Berger, L. Forró, J. Shan, and K. F. Mak, Ising pairing in superconducting $NbSe_2$ atomic layers, Nat. Phys. **12**, 139 (2016).

[54] E. Sohn, X. Xi, W.-Y. He, S. Jiang, Z. Wang, K. Kang, J.-H. Park, H. Berger, L. Forró, K. T. Law, J. Shan, and K. F. Mak, An unusual continuous paramagnetic-limited superconducting phase transition in 2D $NbSe_2$, Nat. Mater. **17**, 504 (2018).

[55] A. Anikin, R. D. Schaller, G. P. Wiederrecht, E. R. Margine, I. I. Mazin, and G. Karapetrov, Ultrafast dynamics in the high-symmetry and in the charge density wave phase of 2*H*-$NbSe_2$, Phys. Rev. B **102**, 205139 (2020).

[56] C.-S. Lian, C. Si, J. Wu, and W. Duan, First-principles study of Na-intercalated bilayer $NbSe_2$: Suppressed charge-density wave and strain-enhanced superconductivity, Phys. Rev. B **96**, 235426 (2017).

[57] J. M. Lu, O. Zheliuk, I. Leermakers, N. F. Q. Yuan, U. Zeitler, K. T. Law, and J. T. Ye, Evidence for two-dimensional Ising superconductivity in gated MoS_2, Science **350**, 1353 (2015).

[58] Y. Saito, Y. Nakamura, M. S. Bahramy, Y. Kohama, J. Ye, Y. Kasahara, Y. Nakagawa, M. Onga, M. Tokunaga, T. Nojima, Y. Yanase, and Y. Iwasa, Superconductivity protected by spin–valley locking in ion-gated MoS_2, Nat. Phys. **12**, 144 (2016).

[59] B. T. Zhou, N. F. Q. Yuan, H.-L. Jiang, and K. T. Law, Ising superconductivity and Majorana fermions in transition-metal dichalcogenides, Phys. Rev. B **93**, 180501(R) (2016).

[60] L. Bawden, S. P. Cooil, F. Mazzola, J. M. Riley, L. J. Collins-McIntyre, V. Sunko, K. W. B. Hunvik, M. Leandersson, C. M. Polley, T. Balasubramanian, T. K. Kim, M. Hoesch, J. W. Wells, G. Balakrishnan, M. S. Bahramy, and P. D. C. King, Spin-valley locking in the normal state of a transition-metal dichalcogenide superconductor, Nat. Commun. **7**, 11711 (2016).

[61] R. Habara and K. Wakabayashi, Optically induced spin current in monolayer $NbSe_2$, Phys. Rev. B **103**, L161410 (2021).

[62] R. Habara and K. Wakabayashi, Nonlinear optical hall effect of few-layered $nbse_2$, Phys. Rev. Res. **4**, 013219 (2022).

[63] See Supplemental Material at http://link.aps.org/supplemental/10.1103/PhysRevB.107.115422 for imaginary parts of NLO conductivities under irradiation of BCL, rotational angle dependencies of BCL on NLO conductivities, derivation of shift- and injection-current conductivities, and NLO conductivity for TMDC semiconductor.

[64] G.-B. Liu, W.-Y. Shan, Y. Yao, W. Yao, and D. Xiao, Three-band tight-binding model for monolayers of group-VIB transition metal dichalcogenides, Phys. Rev. B **88**, 085433 (2013).

[65] S. Kim and Y.-W. Son, Dichotomy of saddle points in energy bands of monolayer $NbSe_2$, Phys. Rev. B **104**, 045426 (2021).

[66] N. L. Kang and S. D. Choi, Derivation of nonlinear optical conductivity by using a reduction identity and a state-dependent projection method, J. Phys. A: Math. Theor. **43**, 165203 (2010).

[67] H. J. Lee, N. L. Kang, J. Y. Sug, and S. D. Choi, Calculation of the nonlinear optical conductivity by a quantum-statistical method, Phys. Rev. B **65**, 195113 (2002).

[68] N. L. Kang, S.-S. Lee, and S. D. Choi, Projection-reduction method applied to deriving non-linear optical conductivity for an electron-impurity system, AIP Adv. **3**, 072104 (2013).

[69] C. Aversa and J. E. Sipe, Nonlinear optical susceptibilities of semiconductors: Results with a length-gauge analysis, Phys. Rev. B **52**, 14636 (1995).

[70] J. E. Sipe and E. Ghahramani, Nonlinear optical response of semiconductors in the independent-particle approximation, Phys. Rev. B **48**, 11705 (1993).

[71] A. Taghizadeh, F. Hipolito, and T. G. Pedersen, Linear and nonlinear optical response of crystals using length and velocity gauges: Effect of basis truncation, Phys. Rev. B **96**, 195413 (2017).

[72] Q. Y. Lu, N. Bandyopadhyay, S. Slivken, Y. Bai, and M. Razeghi, Room temperature single-mode terahertz sources based on intracavity difference-frequency generation in quantum cascade lasers, Appl. Phys. Lett. **99**, 131106 (2011).

[73] A. Ruehl, A. Gambetta, I. Hartl, M. E. Fermann, K. S. E. Eikema, and M. Marangoni, Widely-tunable mid-infrared frequency comb source based on difference frequency generation, Opt. Lett. **37**, 2232 (2012).

[74] F. Mauger, A. D. Bandrauk, and T. Uzer, Circularly polarized molecular high harmonic generation using a bicircular laser, J. Phys. B: At., Mol. Opt. Phys. **49**, 10LT01 (2016).

[75] Z.-Y. Chen, Spectral control of high harmonics from relativistic plasmas using bicircular fields, Phys. Rev. E **97**, 043202 (2018).

[76] A. Gazibegović-Busuladžić, W. Becker, and D. B. Milošević, Helicity asymmetry in strong-field ionization of atoms by a bicircular laser field, Opt. Express **26**, 12684 (2018).

[77] R. D. King-Smith and D. Vanderbilt, Theory of polarization of crystalline solids, Phys. Rev. B **47**, 1651 (1993).

[78] R. Resta, Macroscopic polarization in crystalline dielectrics: the geometric phase approach, Rev. Mod. Phys. **66**, 899 (1994).

[79] N. Marzari, A. A. Mostofi, J. R. Yates, I. Souza, and D. Vanderbilt, Maximally localized Wannier functions: Theory and applications, Rev. Mod. Phys. **84**, 1419 (2012).

[80] H. Watanabe and Y. Yanase, Chiral Photocurrent in Parity-Violating Magnet and Enhanced Response in Topological Antiferromagnet, Phys. Rev. X **11**, 011001 (2021).

[81] Q. Ma, R. Krishna Kumar, S.-Y. Xu, F. H. L. Koppens, and J. C. W. Song, Photocurrent as a multiphysics diagnostic of quantum materials, Nat. Rev. Phys. **5**, 170 (2023).